

# The Vortex State in Geologic Materials: A Micromagnetic Perspective

Ioan Lascu<sup>1,2</sup>, Joshua F. Einsle<sup>2,3</sup>, Matthew R. Ball<sup>2</sup>, Richard J. Harrison<sup>2</sup>

<sup>1</sup>Department of Mineral Sciences, National Museum of Natural History, Smithsonian Institution, Washington, DC, 20560,

United States

<sup>2</sup>Department of Earth Sciences, University of Cambridge, Cambridge, CB2 3EQ, United Kingdom

<sup>3</sup>Department of Materials Sciences and Metallurgy, University of Cambridge, Cambridge, CB3 0FS, United Kingdom

## Key Points:

- Micromagnetic modeling of FORC diagrams are key to understanding vortex phenomena in geologic materials
- Single vortex assemblages have both remanent (notably, a central ridge) and transient FORC fingerprints
- Multi vortex assemblages are important remanence carriers; their FORC fingerprint is a broad central peak

## Abstract

A wide variety of Earth and planetary materials are very good recorders of paleomagnetic information. However most magnetic grains in these materials are not in the stable single (SD) domain grain size range, but are larger and in non-uniform vortex magnetization states. We provide a detailed account of vortex phenomena in geologic materials by simulating first-order reversal curves (FORCs) via finite-element micromagnetic modeling of magnetite nanoparticles with realistic morphologies. The particles have been reconstructed from focused ion beam nanotomography of magnetite-bearing obsidian, and accommodate single and multiple vortex structures. Single vortex (SV) grains have fingerprints with contributions to both the transient and transient-free zones of FORC diagrams. A fundamental feature of the SV fingerprint is a central ridge, representing a distribution of negative saturation vortex annihilation fields. SV irreversible events at multiple field values along different FORC branches determine the asymmetry in the upper and lower lobes of generic bulk FORC diagrams of natural materials with grains predominantly in the vortex state. Multi vortex (MV) FORC signatures are modeled here for the first time. MV grains contribute mostly to the transient-free zone of a FORC diagram, averaging out to create a broad central peak. The intensity of the central peak is higher than that of the lobes, implying that MV particles are more abundant than SV particles in geologic materials with vortex state fingerprints. The abundance of MV particles, as well as their SD-like properties point to MV grains being the main natural remanent magnetization carriers in geologic materials.

## 1 Introduction

Rocks can record information about the geomagnetic field intensity and direction, and preserve it over geologic timescales. Uniformly magnetized, stable single domain (SD) particles are ideal recorders of this information [*Néel*, 1949], and rock magnetic recording mechanisms are widely tied to their presence in natural materials. For magnetite, SD grains are usually a few tens of nm in size in the case of equidimensional particles, and up to 200 nm for elongated particles. Slightly larger particles have non-uniform magnetization states, and have been traditionally classified as pseudo single domain (PSD), because of their transitional properties between SD and larger, multi domain (MD) grains. These intermediate-size grains have the capacity to acquire remanent magnetization efficiently, like SD particles, but have lower coercivities, akin to MD particles [*Stacey*, 1962,

1963]. For PSD magnetite, grain size ranges from around 100 nm to a few  $\mu\text{m}$ , depending on grain morphology. These particles are not uniformly magnetized, but are not partitioned into magnetic domains either. They are mostly found in vortex configurations [e.g., *Shcherbakov et al.*, 1990; *Williams and Dunlop*, 1995]. Since vortex phenomena adequately explain the physics of the magnetization in these particles, *Roberts et al.* [2017] have proposed replacing the term 'PSD state', which is used purely functionally, with 'vortex state'. *Roberts et al.* [2017] presented evidence for single vortex (SV) processes providing the physical explanation for PSD behavior at the fine end of the grain size range, and explored the role of multiple vortices in explaining the physics at the coarse end of the PSD spectrum.

In finite-element micromagnetic calculations, magnetic vortices are the lowest energy states for non-uniformly magnetized particles just above the SD upper threshold [*Williams and Dunlop*, 1995]. Recently, *Almeida et al.* [2016] and *Nagy et al.* [2017] have demonstrated that SV particles can have very high blocking temperatures (close to the Curie point for magnetite) and relaxation times larger than the age of the Earth. Calculations have shown that equidimensional SV magnetite grains up to 1000 nm in size are among the best carriers of remanent magnetization in natural samples [*Nagy et al.*, 2017]. Considering their grain size range, vortex state particles are much more abundant in rocks than SD particles, and they are the main natural remanence carriers in geologic samples. Most rocks do not contain equidimensional SV particles, but are still very good paleomagnetic recorders [e.g., *Carvallo et al.*, 2006; *Smirnov and Evans*, 2015]. These rocks will likely contain a combination of SV grains, some with shape anisotropy [*Einsle et al.*, 2016], and larger grains that accommodate multiple vortices and related micromagnetic configurations [*Roberts et al.*, 2017].

Particles in the vortex state grain size range can be reliably identified using first-order reversal curve (FORC) diagrams, which are sensitive to grain size, domain state, and magnetostatic interactions [*Pike et al.*, 1999; *Roberts et al.*, 2000, 2014]. The vortex state fingerprint in FORC diagrams is distinct from SD and MD fingerprints, representing an intermediate geometry between the high coercivity horizontally spread distribution of the former and the low coercivity vertically spread distribution the latter [*Roberts et al.*, 2014]. *Roberts et al.* [2017] have reasoned that FORC diagrams should be used as a diagnostic tool for the presence of vortex state particles in natural samples, as they are sensitive to the presence of single vortices. They have also recognized that micromagnetic modeling

80 of particles containing multiple vortices is needed in order to paint a complete picture of  
81 the vortex state.

82 The goal of the present article is to model FORC distributions of SV and multi vor-  
83 tex (MV) particles with realistic morphologies (as found in geologic samples), using finite-  
84 element micromagnetic modeling. The only micromagnetic simulations of vortex FORC  
85 diagrams have been performed by *Carvallo et al.* [2003], *Roberts et al.* [2017], and *Valdez-*  
86 *Grijalva* [2018] who have modeled simple SV grain morphologies. No micromagnetic  
87 FORC simulation exists for the MV state. Here, we have reconstructed a  $\mu\text{m}$ -scale volume  
88 from an obsidian sample containing magnetite particles up to several  $\mu\text{m}$  in size, and use  
89 it as input for a micromagnetic model that simulates experimental FORC acquisition pro-  
90 tocols for individual particles. We show that SV and MV micromagnetic configurations  
91 control the geometry of FORC signatures observed experimentally, and that they account  
92 for most of the features observed in samples with particles that span the entire vortex state  
93 grain size continuum.

## 94 **2 Materials and Methods**

95 The specimen investigated in this study is an obsidian fragment from Glass Buttes,  
96 Oregon. Geochemically, it can be ascribed to type C/gamma obsidian, based on character-  
97 istic ratios of Eu/Th, Rb/Sr, and Zr/Ba [*Ambroz et al.*, 2001; *Frahm and Feinberg*, 2015].  
98 FORC acquisition was performed at the University of Cambridge using a Lake Shore Cry-  
99 otronics, Inc. PMC-3900 Series vibrating sample magnetometer. Between 193 and 283  
100 FORCs were collected for each experiment, with a measurement resolution of 1-2 mT.  
101 FORCs were processed in FORCin 3.0 [*Harrison and Feinberg*, 2008], using the VARI-  
102 FORC variable smoothing algorithm of *Egli* [2013]. Low-temperature magnetization was  
103 measured using a Quantum Design Magnetic Properties Measurement System at the Uni-  
104 versity of Cambridge. The sample was cooled in a 2.5 T field from 300 to 20 K, tem-  
105 perature at which the field was switched off and the remanent magnetization measured  
106 on warming back to 300 K in 5 K increments. The sample was subsequently cooled in  
107 zero field from 300 to 20 K, at which temperature a 2.5 T remanent magnetization was  
108 imparted and measured on warming as described above. Magnetic susceptibility was mea-  
109 sured in argon as a function of temperature from 25 to 700 °C, and back to room temper-  
110 ature, using an AGICO MFK1 Kappabridge susceptometer at the University of Cambridge.

111 Three-dimensional reconstruction of a  $\mu\text{m}$ -scale region of interest (MROI) was ac-  
112 complished via nanotomography, performed with a FEI Helios Nanolab dual-beam focused  
113 ion beam–scanning electron microscope (FIB-SEM) at the Wolfson Electron Microscope  
114 Suite, University of Cambridge. FIB-nanotomography (FIB-nT) involves serially milling  
115 through the sample using the FIB and imaging each cross section with the SEM [*Einsle*  
116 *et al.*, 2016, and references therein]. All FIB milling was performed using an accelerat-  
117 ing voltage of 30 kV. The MROI was prepared using ion beam induced deposition (with a  
118 3 nA ion beam current) to lay down a 1  $\mu\text{m}$  thick tungsten pad. The MROI was isolated  
119 from the bulk sample by selectively milling 20  $\mu\text{m}$  deep trenches on three sides of the re-  
120 gion defined by the tungsten pad. The front trench allows full viewing access to the cross-  
121 section and the side trenches minimize re-deposition effects associated with the sequential  
122 milling process. Three linear fiducial marks were created by milling into the tungsten pad,  
123 and then back filling with carbon and capping with tungsten before starting the automated  
124 sequence. This was done to minimize the amount of image drift in the SEM image stack  
125 [*Jones et al.*, 2014]. A second fiducial cross was used to control of the placement of each  
126 slice in the tomographic sequence. Each 10 nm thick tomographic slice was milled away  
127 using a 920 pA ion beam current. All milling was performed at  $52^\circ$  stage tilt, which is  
128 normal to the FIB. Imaging of the cross-sectional cut face was achieved using backscat-  
129 tered electron imaging with the SEM operating in immersion mode at a low accelerating  
130 voltage of 2 kV with a beam current of 86 pA. The resulting three dimensional particle  
131 volumes were reconstructed using a modified version of the protocol described by *Einsle*  
132 *et al.* [2016]. After image denoising using a non-local means filter, the carbon fiducial  
133 marks were used to provide a template based stack alignment. This minimized morpho-  
134 logical errors resulting from fiducial free stack alignment. The binary segmentation of the  
135 images followed the protocol mentioned above.

136 A selection of particles spanning the vortex state grain size range were chosen for  
137 micromagnetic modeling. Particles were cropped from the segmented FIB-nT stack and  
138 converted to tetrahedral finite-element meshes using the software packages Cubit and  
139 Iso2Mesh [*Fang and Boas*, 2009]. Tetrahedral nodes were generated at 5-10 nm intervals,  
140 depending on particle size. Micromagnetic modeling was performed using Micromag-  
141 netic Earth Related Rapid Interpreted Language Laboratory (MERRILL), a micromagnet-  
142 ics package optimized for rock magnetism [*Ó Conbhuí et al.*, 2018]. MERRILL uses a fi-  
143 nite element method / boundary element method to solve for the magnetic scalar potential

144 inside the particle and thereby calculate the demagnetizing energy of the system. Simula-  
 145 tions were performed by minimizing the total magnetic energy using a conjugate gradient  
 146 method, specially adapted to micromagnetic problems. The upper branch of the hysteresis  
 147 loop was obtained for fields from 300 mT to -300 mT, in 5 mT decrements. Each point  
 148 on the upper branch was then used as the initial state for simulating FORC acquisition.  
 149 Reversal curves were obtained using 5 mT field increments. Micromagnetic FORC simula-  
 150 tions were performed on a pair of adjacent grains (gm1 and gm2), respectively in SD and  
 151 SV states at remanence, as well as on 3 MV particles (gm3, gm4, gm5) (Table 1). Four  
 152 FORC protocols were simulated for the gm1-gm2 pair, with the field parallel to 3 orthog-  
 153 onal directions (X, Y, and Z), as well as along the diagonal (D) of the reference system.  
 154 Three FORC protocols were simulated for gm3, with the field parallel to Y, Z, and D. One  
 155 FORC protocol was simulated for each of the other MV particles, with the field parallel  
 156 to Z for gm4 and Y for gm5. Simulated FORCs were then imported in FORCinel 3.0 and  
 157 processed using LOESS smoothing, with a smoothing factor (SF) of 2.5 [*Harrison and*  
 158 *Feinberg, 2008*]. Positive and negative features in the FORC diagram result from evalu-  
 159 ating the slopes of successive FORC branches (i.e.,  $M_j$  and  $M_{j+1}$ , with  $1 \leq j \leq n-1$ ; where  
 160  $n$  is the total number of FORC branches) using the FORC function  $\rho$  [e.g., *Pike et al.*,  
 161 1999]. Features resulting from the evaluation of a pair of successive branches plot along  
 162 a linear path in the FORC diagram defined by the derivative of the difference FORCs with  
 163 respect to the measurement field, i.e.,  $(M_{j+1} - M_j)'$  [*Egli and Winklhofer, 2014*]. Surface  
 164 meshes and individual micromagnetic states are reproduced here using ParaView [*Ahrens*  
 165 *et al., 2005*].

### 166 3 Results

167 The SEM images and reconstructed volume from FIB-nanotomography show a 300-  
 168 500 nm-thick layer formed of particles with dimensions from tens to hundreds of nm in  
 169 size and variable morphologies (Fig. 1). Whereas smaller grains are mostly equidimen-  
 170 sional, larger grains appear to have formed as a result of the coalescence of smaller grains  
 171 during growth, leading to complex flattened and elongated grain morphologies. *Ma et al.*  
 172 [2007] have demonstrated that the Glass Buttes obsidian microstructure consists of many  
 173 such layers of magnetite nanoparticles, which may be locally folded depending on the dy-  
 174 namics of melt flow.

175 An experimental FORC diagram is shown in Fig. 2. The tri-lobate geometry of the  
 176 FORC signature is typical for the vortex state [Roberts *et al.*, 2014]. The upper and lower  
 177 lobes are not symmetrical with respect to the horizontal axis. The upper lobe contours  
 178 intersect the vertical axis at higher absolute values than the lower lobe contours, which  
 179 tend to intersect the vertical axis closer to the origin. The middle lobe is narrower and  
 180 extends along the horizontal axis, but is not centered on it. The lower lobe is flanked by  
 181 two negative regions, which define the shape of its contours, with the negative area be-  
 182 tween the lower lobe and middle lobe being more prominent. Where the three lobes come  
 183 together, there is a broad peak with an intensity a few times larger than that of the lobes.  
 184 The upper and lower lobes are located in zone 1 ( $B > 0, B_r > 0$ ) and zone 2 ( $B < 0, B_r < 0$ ) of  
 185 the FORC diagram, respectively. These zones are associated with transient magnetization  
 186 events, which only exist in the presence of an external field, so will not contribute to the  
 187 remanent magnetization of the sample [Fabian and von Dobeck, 1997; Fabian, 2003;  
 188 Egli and Winklhofer, 2014; Zhao *et al.*, 2017]. The middle lobe, the more prominent neg-  
 189 ative area, and the central peak are located in zone 3 ( $B > 0, B_r < 0$ ) of the FORC diagram,  
 190 and are associated with transient-free magnetization events, and may contribute to the re-  
 191 manent magnetization of the sample [Fabian and von Dobeck, 1997; Fabian, 2003; Egli  
 192 and Winklhofer, 2014; Zhao *et al.*, 2017]. Fig. 2c shows low temperature magnetization  
 193 curves exhibiting a Verwey transition ( $\sim 120$  K), which is a diagnostic feature for mag-  
 194 netite. The transition is not sharp, indicating that the magnetite is partially oxidized. The  
 195 proportion of remanence lost across the Verwey transition is  $\sim 20$ -50% larger for the field  
 196 cooled curve, which is typical for 'PSD' state grains. The susceptibility curves (Fig. 2d)  
 197 exhibit a Curie temperature of  $\sim 580$  °, confirming the main magnetization carrier to be  
 198 magnetite.

### 199 3.1 Single Vortex FORC Simulations

200 To understand each element of the FORC diagram fingerprint, and the processes  
 201 that lead to it, we turn to the micromagnetic models of the particles reconstructed from  
 202 FIB-nanotomography. Even though FORCs were simulated starting at every point on the  
 203 upper hysteresis branch, only a limited number of discreet FORC branches resulted for  
 204 each direction. Individual FORC branches are defined at reversal fields ( $B_r$ ) where an irre-  
 205 versible magnetization event occurs. For the pair of smallest grains (gm1-gm2), there are  
 206 only a limited number of possible features in the FORC diagram. To understand the ori-

gin of these features, we examine the FORC diagram simulated with the field along Y, as it resulted in only 4 distinct FORC branches, and it exhibited the simplest FORC diagram signature (Fig. 3). The FORC branches are labeled  $M_1$  to  $M_4$  in Fig. 3a. The FORC function, plotted in  $(B, B_r)$  space (Fig. 3b), exhibits non-zero features along 3 horizontal paths, corresponding to reversal field values where magnetization jumps have occurred. These paths are labeled  $(M_2 - M_1)'$ ,  $(M_3 - M_2)'$ , and  $(M_4 - M_3)'$  in Fig. 3b.

Both particles (Fig. 3r) are in SD states at saturation. As the field ( $B$ ) is decreased from positive saturation along  $M_1$ , the larger particle transitions from a flower to a curling configuration via coherent moment rotation. By 0.1 T a proto-vortex core starts forming (Fig. 3c) and continues to gradually develop by the same rotation mechanism to the field value of 0.055 T (Fig. 3e). Up to this point the magnetization changes are reversible, and all the FORCs have identical paths to  $M_1$ . The first irreversible transition occurs between 0.055 and 0.05 T, with the vortex fully nucleating (Fig. 3f), i.e., occupying a local energy minimum. Subsequent FORCs follow branch  $M_2$  from 0.05 up to 0.085 T (points f and d in Fig. 3a). On this segment, the vortex core translates in the +X direction, and denucleates at the magnetization jump between 0.08 T (Fig. 3g) and 0.085 T (Fig. 3d).

The difference in the rate of magnetization change along branches  $M_2$  and to  $M_1$  is evaluated using the FORC function (Fig. 3b). The corresponding contribution of this difference plots along the horizontal path between  $B_r = 0.055$  and 0.05 T, and consists of two features, one negative (labeled 1) and one positive (labeled 2), which are proportional to  $(M_2 - M_1)'$ . Feature 1 results from the difference in the slopes of  $M_2$  and  $M_1$  between  $B = 0.055$  and 0.06 T, and is negative because the slope of  $M_1$  is greater than the slope of  $M_2$  on this segment. Feature 2 is a point peak, and is the result of the irreversible magnetization change associated with the annihilation of the positive saturation vortex ( $V^+$ ). This creates a contribution proportional to the Dirac delta function accounting for the irreversible event, which has an amplitude equal to the magnetization jump [Egli and Winkelhofer, 2014]. Peak 2 is positive because the jump occurs on  $M_2$  (i.e., the branch starting from a lower reversal field).

All FORCs starting at reversal fields between 0.05 and  $-0.035$  T coincide with  $M_2$ . As the field is decreased along the upper hysteresis branch, the vortex core progressively translates in the  $-X$  direction (Fig. 3f-j), while the SD particle moments begin to curl (see 0 T configuration, Fig. 3i). The next magnetization jump occurs between  $-0.035$  and



239  $-0.04$  T (Fig. 3j), at the switching field of the SD particle. Subsequent FORCs follow  
 240  $M_3$ , which runs mostly parallel to  $M_2$  up to  $0.035$  T, and then merges with it at the SD  
 241 switching field (Fig. 3h). This jump on  $M_3$ , coupled with no change in the slope of  $M_2$   
 242 between  $B = 0.035$  and  $0.04$  T results in a positive point peak (labeled 3 in Fig. 3b) in the  
 243 FORC diagram between  $B_r = 0.035$  and  $0.04$  T, along path  $(M_3 - M_2)'$ .

244 Decreasing the field along the upper hysteresis branch from  $-0.04$  to  $-0.095$  T (Fig.  
 245 3k), the vortex core continues to translate in the  $-X$  direction. The last FORC branch  
 246 ( $M_4$ ) is accessed between  $-0.095$  and  $-0.1$  T (Fig. 3l), as  $V^+$  is finally annihilated, on  
 247 side of the grain opposite to that on which it nucleated.  $M_4$  coincides with the lower hys-  
 248 teresis branch, and all micromagnetic states and events will mirror those associated with  
 249 the upper hysteresis branch. The negative saturation vortex ( $V^-$ ) develops gradually be-  
 250 tween  $-0.1$  T and  $-0.055$  T (Fig. 3m), with the vortex core fully nucleating at the irre-  
 251 versible jump to  $-0.05$  T (Fig. 3n).  $V^-$  has the same geometry and sense (right-handed)  
 252 as its positive saturation counterpart. The difference is in the orientation of spins, which  
 253 are flipped, giving rise to a vortex configuration with equal net moment and opposite po-  
 254 larity. With progressively increasing fields, the vortex core is being driven out in the  $-X$   
 255 direction, the same as for the upper branch. Switching of the SD particle occurs between  
 256  $0.035$  and  $0.04$  T (Fig. 3p). Finally,  $V^-$  is annihilated between  $0.095$  T (Fig. 3q) and  $0.1$   
 257 T (Fig. 3c).

258 Most of the features of the FORC diagram (labeled 4-9) are along path  $(M_4 - M_3)'$ ,  
 259 between  $B_r = -0.095$  and  $-0.1$  T, representing the evaluation of  $M_4$  against  $M_3$  (Fig.  
 260 3b). Features 4 and 6 are caused by differences in the slopes of the FORCs. Between  $B =$   
 261  $-0.095$  and  $-0.075$  the slope of  $M_3$  is greater, giving rise to feature 4, whereas between  
 262  $-0.045$  and  $-0.035$  the slope of  $M_4$  is greater, giving rise to feature 6. The rest of the  
 263 features are point peaks involving magnetization jumps. Peaks 5 and 9 are positive, as  
 264 the jumps (caused by  $V^-$  nucleating and annihilating, respectively) occur on  $M_4$ . Peak 8  
 265 is negative because the jump (caused by the annihilation of  $V^+$ ) occurs on the previous  
 266 branch ( $M_3$ ). Peak 7 involves magnetization jumps (caused by the SD particle switching)  
 267 on both FORCs, but the amplitude of the jump on  $M_3$  is greater than that of the jump on  
 268  $M_4$ , so the peak is negative. In addition, peak 7 is flanked by negative trails caused by the  
 269 greater slope of  $M_3$  on both sides of the SD switching event.

270 To summarize the distribution of the features in the FORC diagram, features 1 and  
 271 2 plot in zone 1, peaks 4, 5, and 6 in zone 2, and peaks 3, 7, 8, and 9 in zone 3 of the  
 272 FORC diagram (Fig. 3b). In zone 3, peak 3 and peak 9 contribute to the central ridge of  
 273 the FORC diagram (Fig. 4f). Most of these peaks are related to SV irreversible magne-  
 274 tization events, except for Peak 3, which is due to SD switching, and peak 7, which is a  
 275 result of the interplay of SV and SD magnetization phenomena.

276 The FORC diagrams obtained by applying the field along X ( $\text{FORC}_X$ ), Z ( $\text{FORC}_Z$ ),  
 277 and D ( $\text{FORC}_D$ ) are slightly more complex, but are also characterized by only a finite  
 278 number of positive and negative features that contribute to all three zones of the FORC  
 279 diagrams (Fig. 4). In all three field directions some of the FORC branches intersect, pro-  
 280 truding into  $(B, M)$  space that is not accessible to the major hysteresis loop (Fig. 4a,c,d).  
 281 Similar to  $\text{FORC}_Y$  (Fig. 4f), the annihilation of  $V^-$  along the lower branch contributes a  
 282 strong positive peak to the central ridge of  $\text{FORC}_X$  and  $\text{FORC}_D$  (Fig. 4e,g). Due to shape  
 283 anisotropy,  $\text{FORC}_Z$  is in a magnetically hard direction, and the resulting FORC diagram is  
 284 spread out to high field values (Fig. 4h). In addition, we observe a number of peaks that  
 285 cluster around the horizontal axis, representing vortex denucleation fields that do not con-  
 286 tribute to the central ridge. With the field applied along X, gm1 interacts with gm2 such  
 287 that SD switching contributes a peak with a coercivity between 0.075 and 0.08 T that is  
 288 displaced upward from the horizontal axis (Fig. 4e). With the field applied along Z and  
 289 D, gm1 does not interact with gm2, and switches respectively between 0.075 and 0.08 T  
 290 (Fig. 4h), and 0.11 and 0.115 T (Fig. 4g), contributing to the central ridge.

### 291 3.2 Multi Vortex FORC Simulations

292 We investigate the FORC fingerprint of MV particles by focusing on the FORC  
 293 diagram of particle gm3 (Table 1), with the field applied along D (Fig. 5). There are 7  
 294 FORC branches, labeled  $M_1$  to  $M_7$  in Fig. 5a, which yield the main features in the FORC  
 295 diagram (Fig. 5b). The particle (Fig. 5r) is uniformly magnetized at saturation. As the  
 296 field is decreased, the moments start relaxing into local curling configurations (Fig. 5c,d)  
 297 that will serve as nucleation spots for multiple vortex structures. Fig. 5e shows the parti-  
 298 cle at saturation remanence with 5 vortex nucleation sites, two of which are fully nucle-  
 299 ated (lower-right and left sides of the particle) as a result of the irreversible magnetization  
 300 events at the reversal fields corresponding to the beginning of FORC branches  $M_2$  and  $M_3$ .  
 301 In the FORC diagram (Fig. 5b), differences in the slopes of  $M_1$  and  $M_2$ , and of  $M_2$  and

302  $M_3$  produce two positive features in zone 1, respectively along  $(M_2 - M_1)'$  between 0.015  
 303 and 0.02 T (peak 1), and along  $(M_3 - M_2)'$  between 0.05 and 0.055 T (peak 2).

304 The largest irreversible magnetization change on the upper hysteresis branch occurs  
 305 between  $-0.005$  and  $-0.01$  T (Fig. 5a), as the vortices in the center and upper part of  
 306 the particle nucleate, while the other 3 are either annihilated or in the process of denu-  
 307 cleation (e.g., lower right vortex is being driven out in the  $-Z$  direction) (Fig. 5f). With  
 308 increasing field along branch  $M_4$ , the two central vortices start to merge between 0.015  
 309 and 0.02 T, with another vortex core starting to nucleate below it on the left side of the  
 310 particle, while the vortex on the lower right is annihilated (Fig. 5g). Merging of the cores  
 311 of the two central vortices is complete by 0.045 T (Fig. 5h), with the resulting structure  
 312 being annihilated between 0.045 and 0.055 T (Fig. 5d) in two field steps, the first one  
 313 being the most prominent jump. In the FORC diagram, the evolution of these multiple  
 314 vortices is captured via two positive peaks along  $(M_4 - M_3)'$ , marking the jump at 0.02 T  
 315 (peak 3) that results in a configuration with 3 vortex cores on the left side of the particle  
 316 (see Fig. 5g), and the annihilation of the vortices at the large magnetization jump between  
 317  $B = 0.045$  and 0.05 T (peak 4).

318 The next FORC branch,  $M_5$ , is accessed at the jump between  $-0.035$  and  $-0.04$  T.  
 319 The micromagnetic configuration at the reversal field (Fig. 5i) shows the two central vor-  
 320 tices denucleating, and the moments in the upper right side of the particle flipped (now  
 321 pointing in the  $-Y$  direction). The vortex core in the lower right is shifted in the  $+Z$  di-  
 322 rection, and now parallel to  $X$  (compare with Fig. 5f). With increasing field along  $M_5$ ,  
 323 this vortex is being driven out in the  $-Z$  direction, while a large central vortex with an  
 324 elongated, winding core forms as a result of the merger of the previous central vortex  
 325 cores at a jump between 0.005 and 0.01 T (Fig. 5j). The next irreversible event occurs at  
 326 0.035 T (Fig. 5k), when the moments in the upper right part of the particle switch, the  
 327 central vortex structure ends up in the same local energy minimum as on the previous  
 328 FORC (see Fig. 5h), and the lower right vortex is annihilated. After the jump, the paths  
 329 of  $M_5$  and  $M_4$  coincide. In the FORC diagram there are two positive features (labeled 5  
 330 and 6) along  $(M_5 - M_4)'$ . Feature 5 is a double peak associated with the steepening of the  
 331 slope of  $M_5$  between  $-0.005$  and 0.01 T, coupled with no change in the slope of  $M_4$ . Peak  
 332 6 occurs between 0.03 and 0.035 T and marks the merging of the two FORC branches.

333 As the field is decreased from  $-0.04$  T along the upper hysteresis branch, the vortex  
 334 in the lower right is annihilated between  $-0.065$  and  $-0.07$  T via core translation in the  
 335  $+Z$  direction, while a vortex nucleates in the center of the particle, with its core oriented  
 336 along  $Z$  (Fig. 5l). A core nucleation site also begins to develop in upper left part of the  
 337 grain. This micromagnetic state corresponds to the first point on branch  $M_6$ . Along  $M_6$ ,  
 338 the first jump occurs between  $-0.025$  and  $-0.02$  T, field at which the central core is anni-  
 339 hilated and a double vortex nucleates in the lower right of the particle (Fig. 5m). The up-  
 340 per left vortex structure continues to develop, and an additional nucleation site appears in  
 341 the farthest left. The vortex on the left fully nucleates between  $-0.005$  and  $0$  T. At  $0.005$   
 342 T the upper left vortex fully nucleates with an elongated core oriented parallel to  $Y$ , while  
 343 the lower right double vortex is annihilated. This micromagnetic configuration is very  
 344 similar to the one presented in Fig. 5j, and evolves slightly until  $0.03$  T (Fig. 5n), which  
 345 is right before the jump between  $0.03$  and  $0.035$  T that marks the merger of  $M_6$  with  $M_5$   
 346. In the FORC diagram (Fig. 5b) the events occurring on  $M_6$  are evaluated against to the  
 347 ones occurring on  $M_5$  along the path  $(M_6 - M_5)'$ . Peak 7 is due to the jump on  $M_6$  that re-  
 348 sults in the micromagnetic state at  $-0.02$  T (Fig. 5m), coupled with no irreversible change  
 349 on  $M_5$ . Between  $-0.005$  and  $0.035$  T, the positive-negative-positive sequence (peaks 8-  
 350 10) is due to the difference in the slopes of  $M_6$  and  $M_5$ , as follows: between  $-0.005$  and  
 351  $0.005$   $M_6$  is steeper, but due to the jump on  $M_5$  at  $0.01$  T the latter becomes steeper up to  
 352  $0.02$  T, giving peaks 8 and 9 respectively. Between  $0.02$  and  $0.03$  T,  $M_5$  and  $M_6$  are paral-  
 353 lel, with no corresponding signal in the FORC diagram ( $\rho = 0$ ). Peak 10 is a result of the  
 354 jump between  $0.03$  and  $0.035$  T, which has a slightly larger magnitude on  $M_6$  compared to  
 355  $M_5$ .

356  $M_7$  is accessed between  $-0.08$  and  $-0.085$  T, at the last irreversible event along the  
 357 major hysteresis loop, marking the annihilation of the central vortex (see Fig. 5l) and the  
 358 transition of the particle into a flower state. From the reversal point, as the field is in-  
 359 creased along  $M_7$ , the same 5 nucleation sites encountered on the upper hysteresis branch  
 360 will start nucleating vortex structures. From  $-0.085$  to  $-0.005$  T there are two main jumps  
 361 that result in two vortices forming (Fig. 5o): one between  $-0.035$  and  $-0.03$  T (left side)  
 362 and the other between  $-0.01$  and  $-0.005$  T (lower right). The other three nucleation sites  
 363 in Fig. 5o contain proto-cores due to the incipient curling of the moments around those  
 364 sites, but the vortices are not fully nucleated, as the rotation of the moments is reversible.  
 365 The largest irreversible magnetization change occurs between  $0.005$  and  $0.01$  T. The mi-

366 cromagnetic state at 0.01 T (Fig. 5p) shows that the other three vortices have fully nu-  
 367 cleated, while the leftmost vortex has been annihilated. There is an additional jump of  
 368 smaller magnitude between 0.01 and 0.15 T, in which the left side vortices are annih-  
 369 lated, as the moments on this side of the particle that were not oriented in the +Y di-  
 370 rection (blue in Fig. 5p) switch. Between 0.015 and 0.035 T, the two remaining vortices  
 371 (center and lower right) are being driven out, with the central vortex denucleating at the  
 372 irreversible event occurring between 0.035 and 0.04 T (Fig. 5q). Also contributing to this  
 373 jump is the collective switching of moments in the upper right of the particle (red in Fig.  
 374 5q). The lower right vortex is annihilated between 0.065 and 0.07 T, producing the last  
 375 significant jump along  $M_7$ . The nucleation of a central vortex with a core parallel to Z  
 376 and of opposite polarity to its negative counterpart (Fig. 5l) also contributes to the magni-  
 377 tude of this event. This vortex is annihilated between 0.08 and 0.085 T (Fig. 5c).

378 The succession of events occurring on  $M_7$  compared to the ones on  $M_6$  plot at the  
 379 bottom of the FORC diagram along the path  $(M_7 - M_6)'$ . (Fig. 5b). The alternation of  
 380 negative and positive peaks is due to the frequent changes in the slopes of the two reversal  
 381 curves, which creates the interweaved pattern (see Fig. 5a). The first two negative peaks  
 382 (11 and 13) are due to the jumps on  $M_6$  occurring between  $-0.025$  and  $-0.02$  T, and  
 383 between  $-0.005$  and  $0.005$  T. The peaks flank a positive feature (12), which is a double  
 384 peak configuration due to the slope of  $M_7$  being steeper between  $-0.02$  and  $-0.015$  T, and  
 385 between  $-0.01$  and  $-0.005$  T. The most intense positive feature is another double peak  
 386 (14), caused by the sequence of irreversible changes occurring between  $0.005$  and  $0.015$  T  
 387 along  $M_7$ , coupled with no change in slope observed along  $M_6$ . The jump between  $0.03$   
 388 and  $0.035$  T along  $M_6$ , coupled with the jump between  $0.035$  and  $0.04$  T along  $M_7$  trans-  
 389 lates as a pair of negative (peak 15) and positive (peak 16) features, respectively. The  
 390 intense negative feature between  $0.045$  and  $0.055$  T (double peak 17) is due to the large  
 391 two-step irreversible magnetization change along  $M_6$ , couple with no slope change along  
 392  $M_7$ . Finally, the last major jump along  $M_7$ , coupled with no change in the slope of  $M_6$ ,  
 393 gives point peak 18 between  $0.065$  and  $0.07$  T. The majority of the peaks in the FORC di-  
 394 agram (including the highest intensity ones) plot in zone 3 (Fig. 5b), with approximately a  
 395 third of the features plotting in zones 1 and 2.

396 Two additional FORC protocols were simulated by applying the field along Y and  
 397 Z (Fig. 6).  $\text{FORC}_Y$  saturates around  $0.05$  T (Fig. 6b), so it has the most restricted range  
 398 of the three FORC diagrams (Fig. 6e). As with  $\text{FORC}_D$  (Fig. 6d), most of the features

399 associated with the evolution of multiple vortex structures plot in zone 3 of the FORC  
400 diagram (Fig. 6e).  $\text{FORC}_Z$  saturates  $> 0.1$  T and has a wasp-waisted appearance (Fig.  
401 6c). The FORC diagram exhibits a more extensive fingerprint, with peaks distributed in  
402 all three zones (Fig. 6f). Compared to  $\text{FORC}_D$  and  $\text{FORC}_Y$ , there are more features in the  
403 zones 1 and 2 of the  $\text{FORC}_Z$  diagram, which explains the wasp-waisted character of the  
404 major loop.

405 MV FORCs were also simulated for two larger particles, gm4 and gm5 (Table 1).  
406 The large size of the finite element meshes for these particles made the simulations com-  
407 putationally intensive, which did not permit the generation of more than one FORC pro-  
408 tocol for each particle. For gm4 (Fig. 7c), the FORCs were simulated with the field along  
409 Z (Fig. 7a,b), while for gm5 (Fig. 7g), with the field along Y (Fig. 7e,f). The micromag-  
410 netic states of the particles at saturation remanence are shown in Figs. 7d and 7h. Both  
411 particles are characterized by multiple vortex cores, as well as regions of uniform magne-  
412 tization. Almost all of the positive and negative features in the FORC diagram for particle  
413 gm4 are contained in zone 3, with minor contributions to the central ridge. Most of the  
414 features in the FORC diagram of gm5 are also located in zone 3, the main feature being  
415 a very intense positive peak contributing to the central ridge. This peak is due to shape  
416 anisotropy-dictated SD-like switching of the moments in the part of the grain with elon-  
417 gated morphology, between 0.025 and 0.03 T. A second, less intense peak contributes to  
418 the central ridge between 0.055 and 0.6 T, and is due to the SV-like annihilation of the  
419 negative saturation vortex located in the upper left of the particle, which does not interact  
420 with other vortices.

#### 421 **4 Discussion: The Vortex State in Geologic Materials**

422 *Roberts et al.* [2017] have proposed that 'vortex state' replace the term 'PSD state' in  
423 the rock and mineral magnetism nomenclature, because the former provides a meaningful  
424 description of the relevant physics of the dominant magnetization process occurring in this  
425 transitional domain state. SV nucleation and annihilation processes are fairly well under-  
426 stood, and describe the magnetic phenomena observed at the fine end of the vortex state  
427 spectrum. MV-related processes, which account for the magnetic phenomena occurring  
428 at the coarse end of the vortex spectrum, have been explored to a lesser degree. The mi-  
429 cromagnetic simulations presented here from single particles of different sizes and shapes  
430 spanning the SV-MV spectrum offer insight into the processes operating in the magnetic

431 vortex state, and unify the signatures observed in FORC diagrams of materials ranging  
 432 from metallic nanodot arrays [*Pike and Fernandez, 1999; Dumas et al., 2007a,b; Win-*  
 433 *klhofer et al., 2008; Dumas et al., 2009, 2012*] to SV-rich materials [*Lappe et al., 2011,*  
 434 *2013; Zhao et al., 2017*] to PSD-dominated bulk rock samples, such as the obsidian from  
 435 Glass Buttes.

436 Below we synthesize our current understanding of the magnetic vortex state, through  
 437 the lens of FORC diagrams. To illustrate how a handful of FORC diagrams, obtained  
 438 from four vortex state particles in a limited number of field directions, can map the main  
 439 features of the FORC diagram of the bulk specimen from which they were extracted, we  
 440 overlay all the simulated FORC diagrams onto the experimental FORC diagram of the  
 441 Glass Buttes obsidian (Fig. 8). The individual features concentrate in a number of regions  
 442 of the FORC space: positive SV peaks plot onto the upper, lower, and middle lobes; neg-  
 443 ative SV peaks mostly cluster in the negative area between the lower lobe and the middle  
 444 lobe; MV peaks map onto the central peak. A mix of positive and negative features is  
 445 expected throughout the FORC space, with the contribution from the positive peaks out-  
 446 weighing that from the negative peaks in the lobes and central peak, and vice-versa for  
 447 the main negative area of the FORC diagram. This can be readily seen in the relatively  
 448 unsmoothed version of the experimental FORC diagram (Fig. S1). In the main negative  
 449 area (Fig. 8a) the simulated peaks are scarce, due to the limited number of orientations  
 450 and particles modeled, but there is a concentration of negative features at the zero con-  
 451 tour apex, as well as a number of negative peaks in the region where the contour opens  
 452 out. Between these two areas are three positive peaks, two of them from the simulation  
 453 of gm1-gm2 along the hard axis (FORC<sub>Z</sub>). Given the lack of data in this region, it is not  
 454 possible to evaluate the agreement with the experimental data. However, in the positive  
 455 areas, where the data density is higher, the congruence is more than evident. In the lobes  
 456 and central peak areas there is also a mix of positive and negative peaks, but with a clear  
 457 preponderance of positive features. This is in excellent agreement with the experimental  
 458 data.

#### 459 **4.1 Single Vortex Phenomena and Their Fingerprint**

460 SV features contribute to zones 1, 2, and 3 of the FORC diagram. SV features in  
 461 zone 1 are mostly positive peaks associated with the annihilation of the positive saturation  
 462 vortex ( $V^+$ ) along intermediate FORCs (e.g., branch  $M_2$  in Fig. 3a). When  $V^+$  nucleates

463 after a steep decline in magnetization due to the reversible increase in the degree of curl,  
 464 as shown in Fig. 3, the upper hysteresis branch is curved before the magnetization jump,  
 465 and has a higher slope than the FORC branch, leading to a negative peak next to the verti-  
 466 cal axis of the FORC diagram, preceding the positive peak. The coercivity of the positive  
 467 peak is  $(B_{A+}^{V+} - B_N^{V+})/2$ , where  $B_N^{V+}$  is the nucleation field of  $V^+$ , and  $B_{A+}^{V+}$  is the annihila-  
 468 tion field of  $V^+$  along the reversal curve (i.e., with the field increasing). If the nucleation  
 469 occurs after a modest decline in magnetization, so that the FORC branch has a higher  
 470 slope than the upper hysteresis branch, there is no negative peak, and the positive peak  
 471 will be located next to the axis. Since the contours of the upper lobe do not close near the  
 472 origin, the positive contributions must outweigh the negative ones in zone 1, which means  
 473 that vortex nucleation occurs preponderantly without a precursor proto-vortex curling state.

474 In zone 2, the coercivity of SV positive peaks is given by  $(B_N^{V-} - B_{A-}^{V+})/2$ , where  
 475  $B_N^{V-}$  is the nucleation field of the negative saturation vortex ( $V^-$ ), and  $B_{A-}^{V+}$  is the annihila-  
 476 tion field of  $V^+$  along the upper hysteresis branch (i.e., with the field decreasing). This co-  
 477 coercivity is higher than for the positive peak in zone 1 because  $|B_{A+}^{V+}| < |B_{A-}^{V+}|$ . The positive  
 478 peaks are generally preceded by negative features (see Fig. 4e-h), which occur because the  
 479 rate of magnetization change along the lower FORC branch is generally lower than along  
 480 the preceding FORC around  $B_{A-}^{V+}$ . The higher coercivities create the asymmetry between  
 481 the upper and lower lobes, while the presence of negative peaks cause the contours of the  
 482 lower lobe to close near the origin. This configuration has also been observed in FORC  
 483 diagrams of materials dominated by SV particles with a broad grain size distribution span-  
 484 ning hundreds of nm and/or heterogeneous morphologies, such as dusty olivine [Lappe  
 485 *et al.*, 2011, 2013] or hexagonal bacterial platelets Zhao *et al.* [2017]).

486 The main contributions to the upper and lower lobes come from transient irreversible  
 487 events. The two lobes are not restricted to zones 1 and 2. If the nucleation of the positive  
 488 (negative) saturation vortex occurs in negative (positive) field, then the pair positive peaks  
 489 contributing to the lobes will plot instead in zone 3 of the FORC diagram, and will con-  
 490 tribute to remanent magnetization. The lobes can be symmetrical if  $B_{A+}^{V+} = B_{A+}^{V-}$ , where  
 491  $B_{A+}^{V-}$  is the annihilation field of  $V^-$  along the lower branch. However, this happens only in  
 492 very specific circumstances (see Fig. 3d of Dumas *et al.* [2009], and discussion below of  
 493 magnetic disk oriented parallel to the field), and is unlikely to occur in geologic materials.



494 In zone 3, non-interacting SV particles contribute a positive peak to the central  
 495 ridge. Its coercivity is given by  $(B_{A+}^{V-} - B_{A-}^{V+})/2$ . Since for non-interacting SV particles  
 496  $B_{A+}^{V-} = |B_{A-}^{V+}|$ , the coercivity of this peak will be equal to  $B_{A+}^{V-}$ . This is known as inver-  
 497 sion symmetry [Egli and Winklhofer, 2014]. In natural materials, grain size distributions  
 498 are sufficiently broad, so that FORCs do not intersect each other (i.e.,  $B_{A+}^{V+} < B_{A+}^{V-}$ ). This  
 499 results in the central ridge peak being preceded by a negative peak with a coercivity of  
 500  $(B_{A+}^{V-} + B_{A+}^{V+})/2$ . The pairing of these two negative and positive features occurs because  
 501 of the difference in annihilation field values for  $V^+$  and  $V^-$ . This difference is due to the  
 502 vortices annihilating on opposite sides of the particle (compare Figs. 3g and 3q). We thus  
 503 now have the micromagnetic confirmation of the phenomenological model proposed by  
 504 *Pike and Fernandez* [1999] for these features. For weakly-interacting ensembles of natural  
 505 SV particles with random packing, these pairs of positive and negative peaks from indi-  
 506 vidual grains will produce a positive ridge along  $B_c$ , accompanied by a negative trough  
 507 below it [Lappe *et al.*, 2011, 2013; Zhao *et al.*, 2017]. Our modeling results, together with  
 508 observations from such natural SV-dominated materials, lead to the conclusion that a cen-  
 509 tral ridge is a fundamental feature of the SV FORC fingerprint. A SV central ridge is  
 510 distinct from a SD central ridge in three ways: (1) it has a higher median coercivity, be-  
 511 cause the field necessary to reverse a vortex is higher than the field required to switch a  
 512 SD particle or chain of particles; (2) it has approximately the same intensity as the up-  
 513 per and lower lobes, whereas the intensity of a SD ridge is an order of magnitude higher  
 514 than other contributions; and (3) it is adjacent to a negative trough below it, as opposed  
 515 to a positive area above the lower diagonal in the SD case. Our obsidian exhibits a central  
 516 lobe, not a ridge, and a broader, weakly negative area closer to the lower diagonal, rather  
 517 than a trough next to  $B_c$ , so there must be significant inter-particle magnetostatic interac-  
 518 tions that are broadening the ridge and negative trough, and shifting its center below the  
 519 horizontal axis. The advent of variable smoothing has already allowed the identification of  
 520 central ridges in natural samples with vortex FORC fingerprints [Egli, 2013; Ludwig *et al.*,  
 521 2013]

522 If  $B_{A+}^{V+} > B_{A+}^{V-}$ , the lower branch intersects the preceding FORC branch, which  
 523 causes the negative peak to occur after the central ridge peak (i.e., plots above the  $B_c$   
 524 axis). This occurs only in specific circumstances, such as for materials with very narrow  
 525 SV particle size distributions and planar arrangements (e.g., thin films of metallic nan-  
 526 odots). In these materials, some of the lower FORC branches intersect the FORCs of the

527 half loop ( $B > 0$ ) for particular field orientations [*Pike and Fernandez, 1999; Dumas et al.,*  
 528 *2007a,b; Winklhofer et al., 2008; Dumas et al., 2009, 2012*]. This creates a negative trough  
 529 above the central ridge, which generally has a lower intensity than the trough below the  
 530 central ridge. Finally, the rare situation in which there is no SV contribution to the central  
 531 ridge occurs only if  $B_{A+}^{V+} = B_{A+}^{V-}$ , which also results in symmetrical positive contributions  
 532 to zones 1 and 2, as noted above.

533 Prior to micromagnetic modeling efforts, SV features in FORC diagrams have been  
 534 explained using a combined experimental and theoretical approach. In measuring SV  
 535 metallic nanodots with narrow particle size distributions and planar arrangements, vari-  
 536 ous authors have observed the following features in FORC diagrams: two broad, elliptical  
 537 positive peaks in both half planes of the FORC diagram; a negative area next to the  $B_i$   
 538 axis in zone 2; and a high coercivity central ridge paired with a negative trough below it,  
 539 and in some cases a second negative trough above it [*Pike and Fernandez, 1999; Dumas*  
 540 *et al., 2007a,b; Winklhofer et al., 2008; Dumas et al., 2009, 2012*].

541 A further step was taken when the first finite-element micromagnetic simulations  
 542 of SV FORC diagrams were produced. *Carvallo et al. [2003]* modeled a  $100 \times 80 \times 80$  nm  
 543 magnetite parallelepiped, which produced FORCs that follow 5 main branches. These  
 544 branches exhibit random splitting into different sub-branches around the field values at  
 545 which irreversible events occur. This happens when the solution to the minimization al-  
 546 gorithm in the micromagnetic model does not reach equilibrium. The presence of 'hooks'  
 547 at the beginning of many of the reversal curves also supports the premise that these solu-  
 548 tions may have routinely not reached equilibrium. We have observed in our models that  
 549 the number of iterations needed for convergence often surpasses the 'standard' number of  
 550 iterations (5000) by an order of magnitude. Their FORC diagram exhibits multiple posi-  
 551 tive and negative features. However, the SF used was 5, which overly smooths the FORC  
 552 function, and creates averaging over several individual peaks, obscuring contributions from  
 553 discreet irreversible events. In the present study we have used the smallest SF possible  
 554 (2.5), in order to minimize these effects. The large SF used by *Carvallo et al. [2003]* thus  
 555 renders their FORC diagram unsuitable for comparison with the diagrams presented here.

556 *Roberts et al. [2017]* provide the only other instance of finite-element micromagnetic  
 557 modeling of SV FORCs for magnetite. These authors modeled a disk with a diameter of  
 558 240 nm and a thickness of 40 nm, and simulated FORC protocols with the field oriented

559 at angles between  $0^\circ$  and  $90^\circ$  to the plane of the particle, in  $5^\circ$  increments. They noted  
 560 that the main features of their FORC diagrams were two positive peaks of approximately  
 561 the same coercivity, one in the upper half ( $B_i > 0$ ) and one in the lower half ( $B_i < 0$ ) of the  
 562 FORC diagram, which they concluded should be taken as diagnostic signatures for par-  
 563 ticles in the vortex state. Upon closer inspection, their findings are more complex, but  
 564 are nevertheless consistent with our synthesis above. Each of their FORC protocols pro-  
 565 duced between 2 and 4 distinct FORC branches, with the lower branch intersecting the  
 566 preceding branch in some cases. In their FORC diagrams, in addition to the two positive  
 567 peaks, a pair of peaks are present in zone 3, one positive, contributing to the central ridge,  
 568 and one negative. The only exceptions are in the  $0^\circ$  and  $90^\circ$  cases. For the  $0^\circ$  orienta-  
 569 tion,  $B_{A+}^{V-} = B_{A+}^{V+}$ , so the branches coincide at field values  $> B_N^{V-}$ . This creates the special  
 570 case in which the FORC diagram contains no peaks in zone 3, and the two positive peaks  
 571 in the upper and lower FORC half planes have the same coercivities (i.e., are equidistant  
 572 from the  $B_i$  axis). For the  $90^\circ$  orientation, the only feature present is the positive peak on  
 573 the central ridge, because of SD-like switching of the particle. For all other orientations,  
 574  $B_{A+}^{V-}$  is different from  $B_{A+}^{V+}$  (i.e., the branches do not coincide at field values  $> B_N^{V-}$ ). If the  
 575 lower branch does not intersect the preceding branch (as for e.g., the  $60^\circ$  orientation), the  
 576 negative peak in zone 3 plots at  $B_i$  values  $< 0$  (i.e., below the central ridge), while the pos-  
 577 itive peak in the upper FORC half plane has a lower coercivity than the positive peak in  
 578 the lower FORC half plane. If the lower branch intersects the preceding branch (as for  
 579 e.g., the  $30^\circ$  orientation), the negative peak plots at  $B_i$  values  $> 0$  (i.e., above the cen-  
 580 tral ridge), while the positive peak in the upper FORC half plane has a higher coercivity  
 581 than the positive peak in the lower FORC half plane. For most orientations,  $B_N^{V+} > 0$  and  
 582  $B_N^{V-} < 0$ , so the nucleation of  $V+$  and  $V-$  are transient events, and the two positive peaks  
 583 plot in zones 1 and 2 of the FORC diagram. For some orientations (e.g., the  $45^\circ$ ),  $B_N^{V+} < 0$   
 584 and  $B_N^{V-} > 0$ , so the two peaks plot in zone 3, contributing to remanent magnetization.

585 *Valdez-Grijalva* [2018] has modeled the FORC behavior of SV greigite in multiple  
 586 (85-500) random orientations for individual cuboctahedra 60-80 nm in size, and a fram-  
 587 boidal aggregate (composed of tightly packed 30 nm SD particles) that exhibited super-  
 588 vortex behavior. The averaged FORC diagram for the 60-80 nm SV particles have similar  
 589 features to those described here (two positive lobes in each of the FORC half planes and  
 590 a central ridge-like structure accompanied by a negative area below it), indicating that the  
 591 SV FORC fingerprint is diagnostic for both magnetite and greigite. The central ridge-like

592 structure is spread vertically across 10 mT and has a peak that is slightly offset from the  
593 horizontal axis in the negative direction. These effects are due to the fact that the greigite  
594 cuboctahedra are dominated by magnetocrystalline (rather than uniaxial) anisotropy. The  
595 cubic anisotropy creates other FORC signatures in addition to the ones already mentioned:  
596 a strong negative peak at low  $B_c$  and small negative  $B_i$  values, a weak negative region in  
597 the lower left of the FORC diagram, as well as positive and negative diagonal ridges along  
598 the lower diagonal. The greigite framboid composed of tightly-packed (but not touching)  
599 30 nm SD particles was in a super-vortex state at remanence, but its FORC fingerprint  
600 was more akin to MD FORC signatures, with a low coercivity (<20 mT) vertical ridge  
601 extending to  $\pm 80$  mT.

#### 602 **4.2 The Multi Vortex Fingerprint and the MV-MD Transition**

603 *Egli and Winklhofer* [2014] and *Roberts et al.* [2014, 2017] have suggested that SV  
604 features that average out over the FORC space may produce the central peak feature. How-  
605 ever, lobe overlap cannot account for all the signal in the central peak area. In SV-dominated  
606 samples (e.g., dusty olivine [*Lappe et al.*, 2011, 2013], or hexagonal bacterial platelets  
607 [*Zhao et al.*, 2017]), transient irreversible processes account for vortex nucleation events,  
608 resulting in upper and lower lobes that are confined mostly to zones 1 and 2 of the FORC  
609 diagram. No central peak is present in these samples, meaning that SV process alone do  
610 not explain the intensity of central peak in typical natural samples. To explain the central  
611 peak feature, MV processes must be invoked.

612 MV states have been previously documented through imaging and modeling, espe-  
613 cially in the field of materials science [e.g., *Kanda et al.*, 2004; *Elmurodov et al.*, 2006;  
614 *Xu et al.*, 2008; *Gan et al.*, 2014; *Ivanov et al.*, 2016; *Donnelly et al.*, 2017], but also in the  
615 earth and planetary sciences [*Einsle et al.*, 2016; *Roberts et al.*, 2017; *Shah et al.*, 2018].  
616 The key findings of these studies are that MV states are stable in natural and synthetic  
617 materials, and that their remanent magnetizations are higher than for SV states. In natural  
618 materials, MV grains may carry stable magnetizations on time scales comparable to the  
619 age of the solar system [*Shah et al.*, 2018].

620 No finite-element micromagnetic modeling of MV FORCs exists in the literature.  
621 With the present contribution we have taken the first step to fill this void. According to  
622 our simulations, MV features contribute mostly to zone 3, and subordinately to zones 1

623 and 2 of the FORC diagram. In zone 3, MV contributions are distinct from SV contri-  
 624 butions in that they occur at lower coercivities, and are vertically spread, mapping onto  
 625 the central peak feature. MV contributions to the central ridge occur only when there is  
 626 inversion symmetry. This is conditioned by a lack of magnetostatic interactions, such as  
 627 seen for particle gm5, which contains isolated vortices and uniformly magnetized regions  
 628 that switch at the same absolute field value along the upper and lower hysteresis branches.  
 629 This seems to be rare, however, since the central peak is broad, and asymmetric, with a  
 630 maximum intensity displaced from the horizontal axis. Compared to SV particles, MV  
 631 particles must be relatively abundant in geologic materials with predominantly vortex state  
 632 grains, because the central peak has a relatively high intensity compared to that of the  
 633 lobes.

634 The MV reversible and irreversible processes we have documented are core reori-  
 635 entations, translations, and their interactions, including merging of individual cores. As  
 636 the field is decreased along the upper hysteresis branch, we have observed that in general,  
 637 in positive fields, irreversible events contribute to the decrease of net magnetization to a  
 638 lesser degree than in the case of SV simulations. This is likely due to MV intraparticle  
 639 interactions between individual vortices, or between vortices and uniformly magnetized  
 640 regions of a particle. The compound effect of these interactions is that, with decreasing  
 641 field, the system reaches the sequence of major irreversible events after the particle has  
 642 passed through zero field, resulting in high  $M_{rs}/M_s$  values (Table 1, Fig. 8b). The largest  
 643 jumps tend to occur in negative fields, especially in easy magnetic directions, and switch  
 644 back in positive fields (i.e., they are not transient events). Thus, irreversible events occur-  
 645 ring along FORC branches starting at negative  $B_r$  values will contribute to zone 3 of the  
 646 FORC diagram. This mechanism provides an explanation for the SD-like remanent magne-  
 647 tizations of MV particles.

648 The MV fingerprint in FORC diagrams indicates that MV-dominated particles are  
 649 fundamentally different from MD particles. MD FORC fingerprints spread along the  $B_i$   
 650 axis at very low coercivities, whereas MV FORC diagrams resemble those of interacting  
 651 SD particles, which also exhibit a broad peak in zone 3 [Muxworthy and Williams, 2005;  
 652 Harrison and Lascu, 2014]. The transition from MV to MD occurs when the particle is  
 653 large enough, and with a sufficiently large number of micromagnetic states it can adopt,  
 654 that a transition from step-wise to gradual decrease in magnetization occurs as the field is  
 655 decreased from saturation. In this transitional state, domain walls will coexist with vortex

656 cores; this occurs for particle sizes starting at around  $1\ \mu\text{m}$  in equidimensional magnetite  
657 [Nagy *et al.*, 2017; Roberts *et al.*, 2017]. The particles we have modeled are defect-free,  
658 with only shape anisotropy influencing the magnetization states. Natural samples usually  
659 have defects, which can pin domain walls or vortex cores in transitional MV-MD parti-  
660 cles. Defects may divide a MD particle into smaller regions, some of which will behave  
661 effectively like individual vortex particles. The coexistence of domains and SV-like re-  
662 gions may explain the FORC signature of natural MD particles, which retains elements of  
663 the tri-lobate geometry characteristic of SV signatures. This may also explain why FORC  
664 diagrams of materials dominated by MD behavior often exhibit a more pronounced nega-  
665 tive region between the lower and middle lobe than in the case of MV-dominated samples  
666 (e.g., Wright Co. magnetite 3006, with a mean particle size of  $1\ \mu\text{m}$  [Yu, 2002]), which  
667 may lack a negative region altogether.

668 Finally, we caution against the use of the Day diagram [Day *et al.*, 1977] to diagnose  
669 systems containing vortex particles. As can be seen in Fig. 8b, the MV grains used in  
670 the simulations exhibit hysteresis parameters that plot towards the upper left corner, in the  
671 general area classically attributed to SD grains. In contrast, hysteresis parameters for the  
672 SV simulations plot in the lower right corner, in the region designated for MD particles.  
673 For vortex state particles we thus witness an opposite grain size trend to that expected  
674 from a Day diagram. For comparison, the hysteresis parameters of bulk obsidian samples  
675 plot in the PSD region, suggesting a mixture of SV and MV characteristics. MV parti-  
676 cles are abundant in rocks and could be the prime natural remanent magnetization carriers  
677 in geologic materials. The next logical step would be to determine their stability as re-  
678 manence recorders. A number of factors will contribute to this, including particle shape,  
679 structural defects, the number and locations of vortex cores, field direction, magnetization  
680 history, thermal fluctuations, etc. These factors will determine the occurrence and thermal  
681 stability of local energy minima and the magnitude of associated energy barriers.

## 682 **5 Conclusions**

683 1) We have provided a detailed understanding of vortex-related phenomena in ge-  
684 ologic materials by simulating FORCs using finite-element micromagnetic modeling of  
685 magnetite nanoparticles with realistic morphologies. The particles have been reconstructed  
686 from FIB-nanotomography of magnetite-bearing obsidian, and vary in size from  $100\ \text{nm}$   
687 to  $>1\ \mu\text{m}$ , accommodating single and multiple vortex structures. Micromagnetic model-

688 ing of particles with realistic shapes show that modeling vortex phenomena using overly  
689 simplistic models (e.g., double hysteron) are inadequate in understanding vortex behavior.

690 2) Positive and negative features in the FORC diagram result from the evaluation of  
691 the slopes of two successive FORCs. If the slope of a FORC is greater (lesser) than that  
692 of the preceding FORC, indicating a higher (lower) rate of change for the magnetization as  
693 a function of field, the FORC function will be positive (negative). Gradual slope changes  
694 will result in elongated features in the FORC diagram, whereas sudden slope changes,  
695 caused by irreversible magnetization jumps, will translate as point peaks.

696 3) SV grains have FORC fingerprints with contributions in both the transient and  
697 transient-free zones of the FORC diagram. A fundamental feature of the SV fingerprint  
698 is a central ridge, accompanied by a negative trough below it. This stems from individ-  
699 ual non-interacting SV grains contributing positive peaks along the coercivity axis of the  
700 FORC diagram, which are preceded by negative peaks. The positive-negative pairing oc-  
701 curs due to  $V^-$  annihilating along the lower hysteresis branch at a higher field value than  
702  $V^+$  along the preceding FORC branch. SV central ridges are thus distributions of  $V^-$  anni-  
703 hilation fields, and usually have higher median coercivities than SD central ridges, which  
704 are distributions of SD switching fields. SV nucleation-annihilation events at multiple field  
705 values along different branches (caused mainly by the annihilation of  $V^+$  and  $V^-$  on dif-  
706 ferent sides of the particle) also determine the asymmetry in the upper and lower lobes of  
707 generic bulk FORC diagrams of natural materials with grains predominantly in the vortex  
708 state.

709 4) We have modeled MV FORC signatures for the first time. MV grains contribute  
710 mostly to the transient-free zone of a FORC diagram. Due to their larger size, multiple  
711 micromagnetic states they can adopt, and intraparticle interactions, MV grains contribute  
712 positive and negative peaks that are spread vertically, which for large populations of par-  
713 ticles average out to create the broad central peak in the FORC diagram. The intensity  
714 of the central peak is generally higher than that of the lobes, implying that MV particles  
715 are more abundant than SV particles in geologic materials with vortex state fingerprints.  
716 This is of high importance because MV grains could then be the prime natural remanent  
717 magnetization carriers in rocks. Finally, based on the similarities between the FORC fin-  
718 gerprints of strongly interacting SD and MV particles, we propose that widely documented  
719 SD-like moments in geologic vortex state samples are due to MV, not SD grains.

720 **Acknowledgments**

721 This research has received funding from the European Research Council under the Eu-  
722 ropean Union's Seventh Framework Programme (FP/2007-2013)/ERC grant agreement  
723 320750. The mesh files used to generate the data in this paper are available as support-  
724 ing information. We thank James A. Miller for providing the obsidian specimens and Wyn  
725 Williams for assistance with MERRILL. We are grateful to Ramon Egli, Adrian Mux-  
726 worthy, Valera Shcherbakov, and Lesleis Nagy for providing constructive reviews that im-  
727 proved the quality of this paper.



728

**Table 1.** Particle characterization

Particle ID	Morphology	Volume ( $\mu\text{m}^3$ )	DEVS <sup>a</sup> (nm)	Domain state <sup>b</sup>	$M_{rs}/M_s$ <sup>c</sup>
gm1	uniaxial	0.00006	24	SD	
gm2	equidimensional	0.012	290	SV	-0.018 (X)* 0.029 (Y)* 0.015 (Z)* 0.006 (D)*
gm3	flattened	0.022	350	MV	0.070 (X) 0.276 (Y) 0.287 (Z) 0.283 (D)
gm4	flattened	0.039	414	MV	0.043 (X) 0.589 (Y) 0.394 (Z) 0.433 (D)
gm5	elongated	0.076	526	MV	0.033 (X) 0.559 (Y) 0.446 (Z)

<sup>a</sup> diameter of equivalent volume sphere<sup>b</sup> from micromagnetic configuration in zero field: SD-single domain, SV-single vortex, MV-multi vortex<sup>c</sup> saturation remanence ratio, corresponding to field direction in parentheses

\* values for gm1-gm2 ensemble

729

**Figure Captions**

730

731

732

733

734

Figure 1. Magnetite layer in Glass Buttes obsidian. a) Examples of imagery acquired during the FIB slice and view protocol. b) Two views of the volume reconstructed via FIB-nanotomography. Particle sizes vary from  $\sim 100$  nm to  $>1$   $\mu\text{m}$ . The larger particles have formed through coalescence of smaller grains from neighboring nucleation sites during crystal growth.

735

736

Figure 2. a) FORC measurements of Glass Buttes obsidian sample. For clarity, only every 5th FORC is plotted. b) FORC diagram resulting from processing the FORCs in (a)

737 using the following smoothing parameters:  $s_{c,0} = s_{b,0} = 9$ ,  $s_{c,1} = s_{b,1} = 9$ ,  $\lambda = 0.2$ .  
 738 Contour interval is  $10^{-6} \text{ Am}^2/\text{T}^2$ . Dashed contour delineates regions of the FORC distri-  
 739 bution significant at the 0.05 level [Heslop and Roberts, 2012]. See text for description of  
 740 the component features of the FORC fingerprint and the zones they occupy (labeled 1, 2,  
 741 and 3). The three zones are delimited by the diagonals of the FORC diagram, which rep-  
 742 resent the  $(B, B_r)$  coordinates. c) Low temperature 2.5 T remanence measured on warming  
 743 after two different pretreatments: cooling in field (FC) and cooling in zero field (ZFC). d)  
 744 Magnetic susceptibility as a function of temperature.

745 Figure 3. Micromagnetic FORC simulation of the gm1-gm2 ensemble with the field  
 746 applied along Y. a) Simulated FORCs: the 4 branches are labeled  $M_1$  to  $M_4$ . Letters indi-  
 747 cate panels corresponding to micromagnetic states at positions marked by black dots.  $B_N$   
 748 is the nucleation field, while  $B_{A+}$  and  $B_{A-}$  are annihilation fields along ascending and de-  
 749 scending branches, respectively. The  $V+$  and  $V-$  superscripts represent the positive and  
 750 negative saturation vortices. b) FORC diagram, processed using simple smoothing, with  
 751  $\text{SF} = 2.5$ . Positive and negative features (labeled 1-9, discussed in text) plot along three  
 752 horizontal paths, labeled  $(M_2 - M_1)'$ ,  $(M_3 - M_2)'$ , and  $(M_4 - M_3)'$ , located at reversal  
 753 fields  $(B_r)$  where magnetization jumps have occurred. The diagonals of the diagram are  
 754 the  $B_c$  and  $B_i$  axes. c-q) Micromagnetic states corresponding to field values labeled in (a).  
 755 Surfaces (green) delineate vortex cores. r) Meshes of gm1 and gm2, and their orientation:  
 756 the Y and Z directions are at  $45^\circ$  to the plane of the figure (i.e., the view is parallel to the  
 757 diagonal of the (Y,Z) coordinate plane, which points into the figure plane.

758 Figure 4. Simulated FORCs (a-d) and FORC diagrams (e-h) of the gm1-gm2 ensem-  
 759 ble along four field directions: X (a, e), Y (b, f), Z (c, g), and D (d, h). Direction D is the  
 760 diagonal of the coordinate system plotted in Fig. 3.  $\text{SF} = 2.5$ .

761 Figure 5. Micromagnetic FORC simulation of particle gm3 with the field applied  
 762 along D. a) Simulated FORCs: the 7 branches are labeled  $M_1$  to  $M_7$ . Letters indicate pan-  
 763 els corresponding to micromagnetic states at positions marked by black dots. b) FORC  
 764 diagram, processed using simple smoothing, with  $\text{SF} = 2.5$ . Positive and negative fea-  
 765 tures (labeled 1-18, discussed in text) plot along 6 horizontal paths (labeled  $(M_{j+1} - M_j)'$ ,  
 766  $1 \leq j \leq 6$ ) located at reversal fields  $(B_r)$  where magnetization jumps have occurred. The di-  
 767 agonals of the diagram are the  $B_c$  and  $B_i$  axes. c-q) Micromagnetic states corresponding

768 to field values labeled in (a). Surfaces (green) delineate vortex cores. r) Mesh of particle  
769 gm3. The view is parallel to X, which points into the figure plane.

770 Figure 6. Simulated FORCs (a-c) and FORC diagrams (d-f) of particle gm3 along  
771 three field directions: D (a, d), Y (b, e), and Z (c, f). Direction D is the diagonal of the  
772 coordinate system, as seen in Fig. 5. SF = 2.5.

773 Figure 7. FORC simulations of particles gm4 (a-d, field applied along Z) and gm5  
774 (e-h, field applied along Y): FORCs (a, e), FORC diagrams (b, f), particle meshes (c, g),  
775 and micromagnetic states at saturation remanent magnetization,  $M_{rs}$  (d, h). SF = 2.5.

776 Figure 8. a) Positive and negative features from the all the FORC diagrams simu-  
777 lated in this study superimposed onto the contours of the experimental FORC diagram  
778 shown in Fig. 2. b) Day diagram of the nine simulations and six obsidian samples. Dashed  
779 ellipse indicates the range of values for Wright Co. magnetite 3006 (mean grain size 1  
780  $\mu\text{m}$ ) hysteresis parameters [Yu, 2002; Carter-Stiglitz et al., 2001; Dunlop and Carter-Stiglitz,  
781 2006; Harrison et al., 2018].

## 782 References

- 783 Ahrens, J., B. Geveci, C. Law, C. Hansen, and C. Johnson (2005), Paraview: An end-user  
784 tool for large-data visualization, in *The visualization handbook*, edited by C. D. Hansen  
785 and C. R. Johnson, pp. 717–732, Elsevier.
- 786 Almeida, T. P., A. R. Muxworthy, A. Kovács, W. Williams, P. D. Brown, and R. E. Dunin-  
787 Borkowski (2016), Direct visualization of the thermomagnetic behavior of pseudo-  
788 single-domain magnetite particles, *Science Advances*, 2(4), doi:10.1126/sciadv.1501801.
- 789 Ambroz, J. A., M. D. Glascock, and C. E. Skinner (2001), Chemical differentiation of  
790 obsidian within the Glass Buttes complex, Oregon, *Journal of Archaeological Science*,  
791 28(7), 741–746, doi:10.1006/jasc.2000.0593.
- 792 Carter-Stiglitz, B., B. Moskowitz, and M. Jackson (2001), Unmixing magnetic assem-  
793 blages and the magnetic behavior of bimodal mixtures, *Journal of Geophysical Re-  
794 search*, 106(B11), 26,397–26,411, doi:10.1029/2001JB000417.
- 795 Carvalho, C., A. R. Muxworthy, D. J. Dunlop, and W. Williams (2003), Micromagnetic  
796 modeling of first-order reversal curve (FORC) diagrams for single-domain and pseudo-  
797 single-domain magnetite, *Earth and Planetary Science Letters*, 213(3-4), 375–390, doi:  
798 10.1016/S0012-821X(03)00320-0.

- 799 Carvallo, C., A. R. Muxworthy, and D. J. Dunlop (2006), First-order reversal curve  
800 (FORC) diagrams of magnetic mixtures: Micromagnetic models and mea-  
801 surements, *Physics of the Earth and Planetary Interiors*, *154*(3), 308–322, doi:  
802 10.1016/j.pepi.2005.06.017.
- 803 Day, R., M. Fuller, and V. Schmidt (1977), Hysteresis properties of titanomagnetites:  
804 Grain-size and compositional dependence, *Physics of the Earth and Planetary Interiors*,  
805 *13*(4), 260–267, doi:10.1016/0031-9201(77)90108-X.
- 806 Donnelly, C., M. Guizar-Sicairos, V. Scagnoli, S. Gliga, M. Holler, J. Raabe, and L. J.  
807 Heyderman (2017), Three-dimensional magnetization structures revealed with X-ray  
808 vector nanotomography, *Nature*, *547*, 328–331, doi:10.1038/nature23006.
- 809 Dumas, R. K., K. Liu, C.-P. Li, I. V. Roshchin, and I. K. Schuller (2007a), Tempera-  
810 ture induced single domain–vortex state transition in sub-100 nm fe nanodots, *Applied*  
811 *Physics Letters*, *91*(20), 202,501, doi:10.1063/1.2807276.
- 812 Dumas, R. K., C.-P. Li, I. V. Roshchin, I. K. Schuller, and K. Liu (2007b), Mag-  
813 netic fingerprints of sub-100 nm fe nanodots, *Physical Review B*, *75*, 134,405, doi:  
814 10.1103/PhysRevB.75.134405.
- 815 Dumas, R. K., T. Gredig, C.-P. Li, I. K. Schuller, and K. Liu (2009), Angular dependence  
816 of vortex-annihilation fields in asymmetric cobalt dots, *Physical Review B*, *80*, 014,416,  
817 doi:10.1103/PhysRevB.80.014416.
- 818 Dumas, R. K., C.-P. Li, I. V. Roshchin, I. K. Schuller, and K. Liu (2012), Deconvolut-  
819 ing reversal modes in exchange-biased nanodots, *Physical Review B*, *86*, 144,410, doi:  
820 10.1103/PhysRevB.86.144410.
- 821 Dunlop, D. J., and B. Carter-Stiglitz (2006), Day plots of mixtures of superparamagnetic,  
822 single-domain, pseudosingle-domain, and multidomain magnetites, *Journal of Geophysi-  
823 cal Research*, *111*(B12), B12S09, doi:10.1029/2006JB004499.
- 824 Egli, R. (2013), VARIFORC: An optimized protocol for calculating non-regular first-order  
825 reversal curve (FORC) diagrams, *Global and Planetary Change*, *110*, 302–320, doi:  
826 10.1016/j.gloplacha.2013.08.003.
- 827 Egli, R., and M. Winklhofer (2014), Recent developments on processing and interpretation  
828 aspects of first-order reversal curves (FORC), *Proceedings of Kazan University*, *156*, 14–  
829 53.
- 830 Einsle, J. F., R. J. Harrison, T. Kasama, P. Ó. Conbhuí, K. Fabian, W. Williams, L. Wood-  
831 land, R. R. Fu, B. P. Weiss, and P. A. Midgley (2016), Multi-scale three-dimensional

- 832 characterization of iron particles in dusty olivine: Implications for paleomagnetism of  
 833 chondritic meteorites, *American Mineralogist*, 101(9), 2070–2084, doi:10.2138/am-2016-  
 834 5738CCBY.
- 835 Elmurodov, A. K., D. Y. Vodolazov, and F. M. Peeters (2006), The break-up of the vortex  
 836 structure in a mesoscopic wire containing a constriction, *Europhysics Letters*, 74(1),  
 837 151, doi:10.1209/epl/i2005-10496-0.
- 838 Fabian, K. (2003), Some additional parameters to estimate domain state from isothermal  
 839 magnetization measurements, *Earth and Planetary Science Letters*, 213(3), 337 – 345,  
 840 doi:10.1016/S0012-821X(03)00329-7.
- 841 Fabian, K., and T. von Dobeneck (1997), Isothermal magnetization of samples with sta-  
 842 ble Preisach function: A survey of hysteresis, remanence, and rock magnetic param-  
 843 eters, *Journal of Geophysical Research: Solid Earth*, 102(B8), 17,659–17,677, doi:  
 844 10.1029/97JB01051.
- 845 Fang, Q., and D. A. Boas (2009), Tetrahedral mesh generation from volumetric binary and  
 846 grayscale images, in *2009 IEEE International Symposium on Biomedical Imaging: From*  
 847 *Nano to Macro*, pp. 1142–1145, doi:10.1109/ISBI.2009.5193259.
- 848 Frahm, E., and J. M. Feinberg (2015), Reassessing obsidian field relationships at  
 849 Glass Buttes, Oregon, *Journal of Archaeological Science: Reports*, 2, 654–665, doi:  
 850 10.1016/j.jasrep.2014.11.007.
- 851 Gan, W. L., M. C. Sekhar, D. W. Wong, I. Purnama, S. Y. Chiam, L. M. Wong, and W. S.  
 852 Lew (2014), Multi-vortex states in magnetic nanoparticles, *Applied Physics Letters*,  
 853 105(15), 152,405, doi:10.1063/1.4898349.
- 854 Harrison, R. J., and J. M. Feinberg (2008), FORCinel: An improved algorithm for calcu-  
 855 lating first-order reversal curve distributions using locally weighted regression smooth-  
 856 ing, *Geochemistry, Geophysics, Geosystems*, 9(5), Q05,016, doi:10.1029/2008GC001987.
- 857 Harrison, R. J., and I. Lascu (2014), FORCulator: A micromagnetic tool for simulating  
 858 first-order reversal curve diagrams, *Geochemistry, Geophysics, Geosystems*, 15(12),  
 859 4671–4691, doi:10.1002/2014GC005582.
- 860 Harrison, R. J., J. Muraszko, D. Heslop, I. Lascu, A. R. Muxworthy, and A. P. Roberts  
 861 (2018), An improved algorithm for unmixing first-order reversal curve diagrams using  
 862 principal component analysis, *Geochemistry, Geophysics, Geosystems*, 19(5), 1595–1610,  
 863 doi:10.1029/2018GC007511.

- 864 Heslop, D., and A. P. Roberts (2012), A method for unmixing magnetic hystere-  
865 sis loops, *Journal of Geophysical Research: Solid Earth*, *117*(B3), B03,103, doi:  
866 10.1029/2011JB008859.
- 867 Ivanov, Y. P., A. Chuvilin, L. G. Vivas, J. Kosel, O. Chubykalo-Fesenko, and M. Vázquez  
868 (2016), Single crystalline cylindrical nanowires—toward dense 3D arrays of magnetic  
869 vortices, *Scientific Reports*, *6*, 23,844, doi:10.1038/srep23844.
- 870 Jones, H., K. Mingard, and D. Cox (2014), Investigation of slice thickness and shape  
871 milled by a focused ion beam for three-dimensional reconstruction of microstructures,  
872 *Ultramicroscopy*, *139*, 20 – 28, doi:10.1016/j.ultramic.2014.01.003.
- 873 Kanda, A., B. J. Baelus, F. M. Peeters, K. Kadowaki, and Y. Ootuka (2004), Experimental  
874 evidence for giant vortex states in a mesoscopic superconducting disk, *Physical Review  
875 Letters*, *93*, 257,002, doi:10.1103/PhysRevLett.93.257002.
- 876 Lappe, S.-C. L. L., N. S. Church, T. Kasama, A. B. da Silva Fanta, G. Bromiley, R. E.  
877 Dunin-Borkowski, J. M. Feinberg, S. Russell, and R. J. Harrison (2011), Mineral mag-  
878 netism of dusty olivine: A credible recorder of pre-accretionary remanence, *Geochem-  
879 istry, Geophysics, Geosystems*, *12*(12), n/a–n/a, doi:10.1029/2011GC003811.
- 880 Lappe, S.-C. L. L., J. M. Feinberg, A. Muxworthy, and R. J. Harrison (2013), Comparison  
881 and calibration of nonheating paleointensity methods: A case study using dusty olivine,  
882 *Geochemistry, Geophysics, Geosystems*, *14*(7), 2143–2158, doi:10.1002/ggge.20141.
- 883 Ludwig, P., R. Egli, S. Bishop, V. Chernenko, T. Frederichs, G. Rugel, S. Merchel, and  
884 M. Orgeira (2013), Characterization of primary and secondary magnetite in marine sed-  
885 iment by combining chemical and magnetic unmixing techniques, *Global and Planetary  
886 Change*, *110*, 321–339, doi:10.1016/j.gloplacha.2013.08.018.
- 887 Ma, C., G. R. Rossman, and J. A. Miller (2007), The origin of color in "fire" obsidian,  
888 *Canadian Mineralogist*, *45*, 551–557, doi:10.2113/gscanmin.45.3.551.
- 889 Muxworthy, A., and W. Williams (2005), Magnetostatic interaction fields in first-  
890 order-reversal-curve diagrams, *Journal of Applied Physics*, *97*(6), 063905, doi:  
891 <http://dx.doi.org/10.1063/1.1861518>.
- 892 Nagy, L., W. Williams, A. R. Muxworthy, K. Fabian, T. P. Almeida, P. Ó. Conbhuí, and  
893 V. P. Shcherbakov (2017), Stability of equidimensional pseudo–single-domain magnetite  
894 over billion-year timescales, *Proceedings of the National Academy of Sciences*, *114*(39),  
895 10,356–10,360.

- 896 Néel, L. (1949), Théorie du trainage magnétique des ferromagnétiques en grains fines avec  
897 applications aux terres cuites, *Annales de Géophysique*, 5, 99–136.
- 898 Ó Conbhuí, P., W. Williams, K. Fabian, P. Ridley, L. Nagy, and A. R. Muxworthy (2018),  
899 MERRILL: Micromagnetic Earth Related Robust Interpreted Language Laboratory,  
900 *Geochemistry, Geophysics, Geosystems*, doi:10.1002/2017GC007279.
- 901 Pike, C., and A. Fernandez (1999), An investigation of magnetic reversal in submicron-  
902 scale Co dots using first order reversal curve diagrams, *Journal of Applied Physics*,  
903 85(9), 6668–6676, doi:10.1063/1.370177.
- 904 Pike, C. R., A. P. Roberts, and K. L. Verosub (1999), Characterizing interactions in fine  
905 magnetic particle systems using first order reversal curves, *Journal of Applied Physics*,  
906 85(9), 6660–6667.
- 907 Roberts, A. P., C. R. Pike, and K. L. Verosub (2000), First-order reversal curve diagrams:  
908 A new tool for characterizing the magnetic properties of natural samples, *Journal of*  
909 *Geophysical Research*, 105(B12), 28,461, doi:10.1029/2000JB900326.
- 910 Roberts, A. P., D. Heslop, X. Zhao, and C. R. Pike (2014), Understanding fine magnetic  
911 particle systems through use of first-order reversal curve diagrams, *Reviews of Geo-*  
912 *physics*, 52(4), 557–602, doi:10.1002/2014RG000462.
- 913 Roberts, A. P., T. P. Almeida, N. S. Church, R. J. Harrison, D. Heslop, Y. Li, J. Li, A. R.  
914 Muxworthy, W. Williams, and X. Zhao (2017), Resolving the origin of pseudo-single  
915 domain magnetic behavior, *Journal of Geophysical Research: Solid Earth*, 122, doi:  
916 10.1002/2017JB014860, 2017JB014860.
- 917 Shah, J., W. Williams, T. P. Almeida, L. Nagy, A. R. Muxworthy, A. Kovács, M. A.  
918 Valdez-Grijalva, K. Fabian, S. S. Russell, M. J. Genge, and R. E. Dunin-Borkowski  
919 (2018), The oldest magnetic record in our solar system identified using nanomet-  
920 ric imaging and numerical modeling, *Nature Communications*, 9(1), 1173, doi:  
921 10.1038/s41467-018-03613-1.
- 922 Shcherbakov, V., P. Schmidt, N. Sycheva, and B. Lamash (1990), Micromagnetic formula-  
923 tion for the personal computer, *Physics of the Earth and Planetary Interiors*, 65(1), 15 –  
924 27, doi:10.1016/0031-9201(90)90071-5.
- 925 Smirnov, A. V., and D. A. Evans (2015), Geomagnetic paleointensity at 2.41 Ga as  
926 recorded by the Widgiemooltha Dike Swarm, Western Australia, *Earth and Planetary*  
927 *Science Letters*, 416, 35–45, doi:10.1016/j.epsl.2015.02.012.

- 928 Stacey, F. (1963), The physical theory of rock magnetism, *Advances in Physics*, 12(45),  
929 45–133, doi:10.1080/00018736300101263.
- 930 Stacey, F. D. (1962), A generalized theory of thermoremanence, covering the transition  
931 from single domain to multi-domain magnetic grains, *Philosophical Magazine*, 7(83),  
932 1887–1900, doi:10.1080/14786436208213853.
- 933 Valdez-Grijalva, M. A. (2018), A numerical investigation of hydrocarbon related magnetic  
934 signatures, Ph.D. thesis, Imperial College London.
- 935 Williams, W., and D. J. Dunlop (1995), Simulation of magnetic hysteresis in pseudo-  
936 single-domain grains of magnetite, *Journal of Geophysical Research: Solid Earth*,  
937 100(B3), 3859–3871, doi:10.1029/94JB02878.
- 938 Winklhofer, M., R. K. Dumas, and K. Liu (2008), Identifying reversible and irreversible  
939 magnetization changes in prototype patterned media using first- and second-order rever-  
940 sal curves, *Journal of Applied Physics*, 103(7), 07C518, doi:10.1063/1.2837888.
- 941 Xu, B., M. V. Milošević, and F. M. Peeters (2008), Magnetic properties of vor-  
942 tex states in spherical superconductors, *Physical Review B*, 77, 144,509, doi:  
943 10.1103/PhysRevB.77.144509.
- 944 Yu, Y. (2002), Partial anhysteretic remanent magnetization in magnetite 1. Additivity,  
945 *Journal of Geophysical Research*, 107(B10), 2244, doi:10.1029/2001JB001249.
- 946 Zhao, X., A. P. Roberts, D. Heslop, G. A. Paterson, Y. Li, and J. Li (2017), Magnetic do-  
947 main state diagnosis using hysteresis reversal curves, *Journal of Geophysical Research*,  
948 122(7), 4767–4789, doi:10.1002/2016JB013683, 2016JB013683.



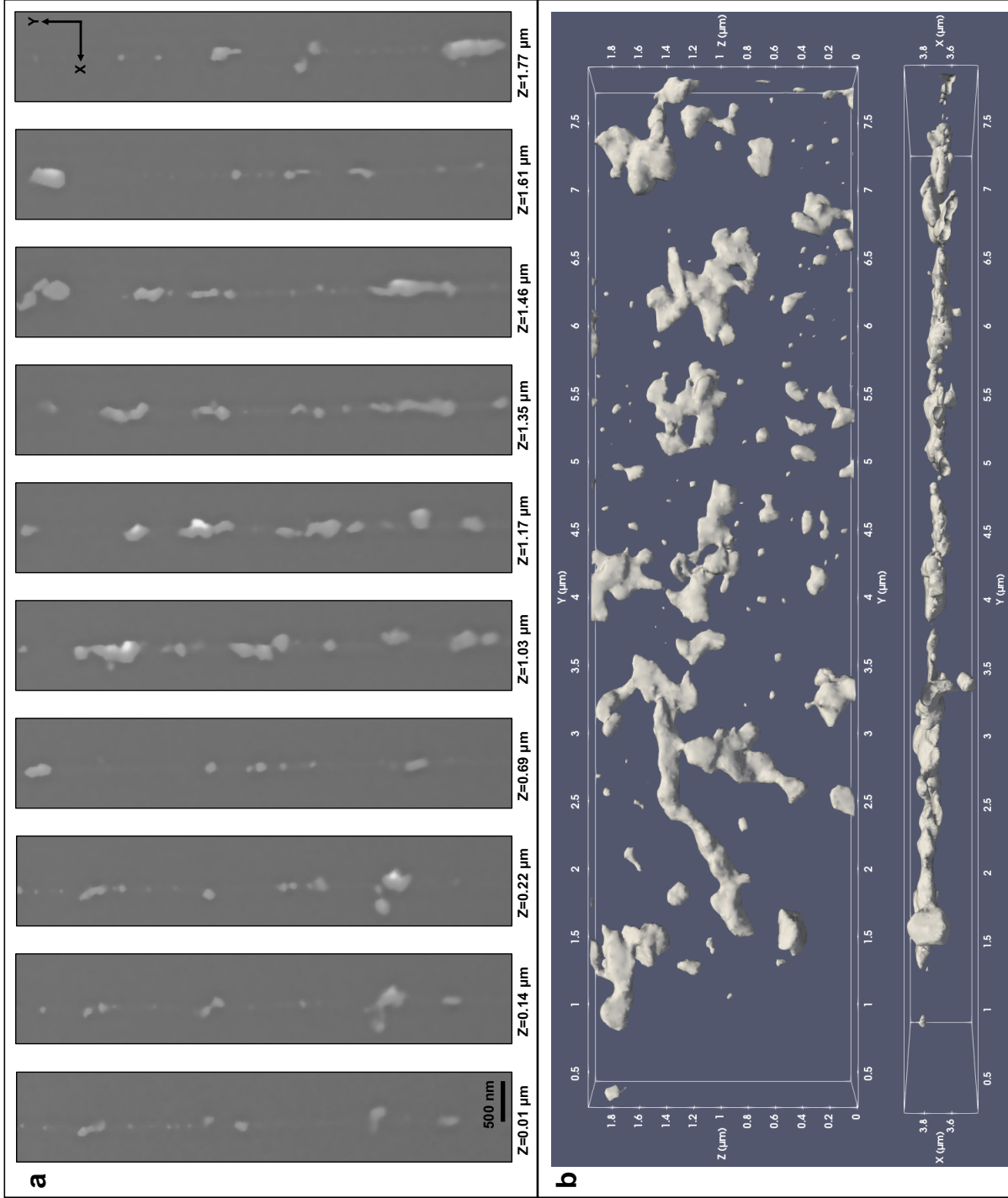
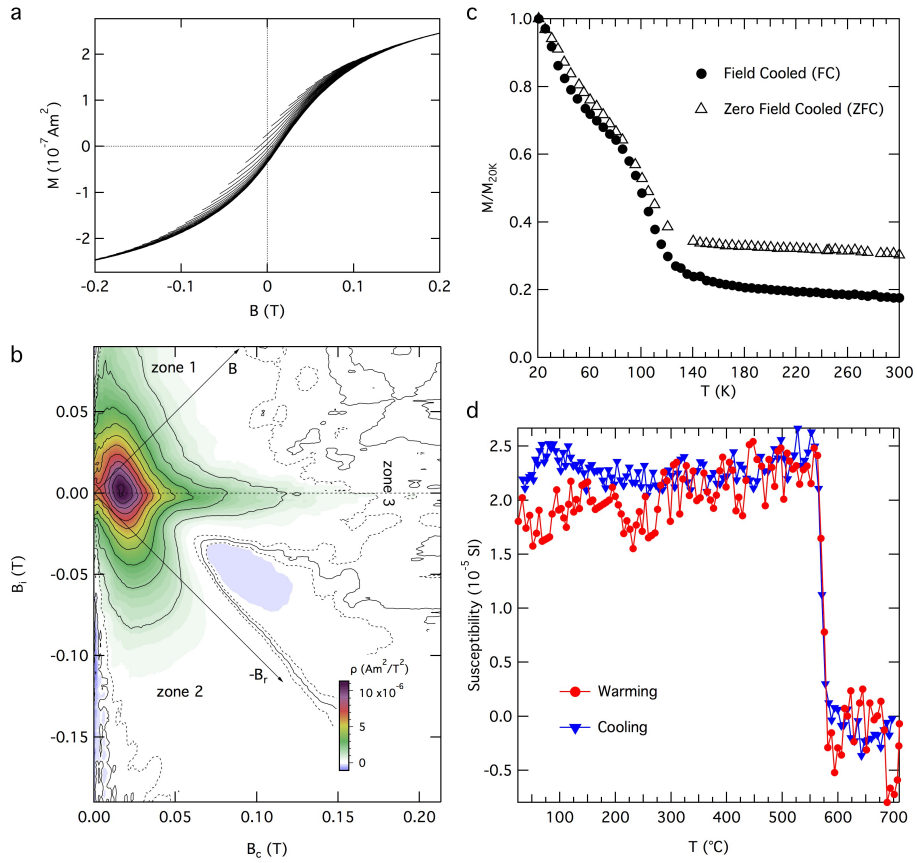
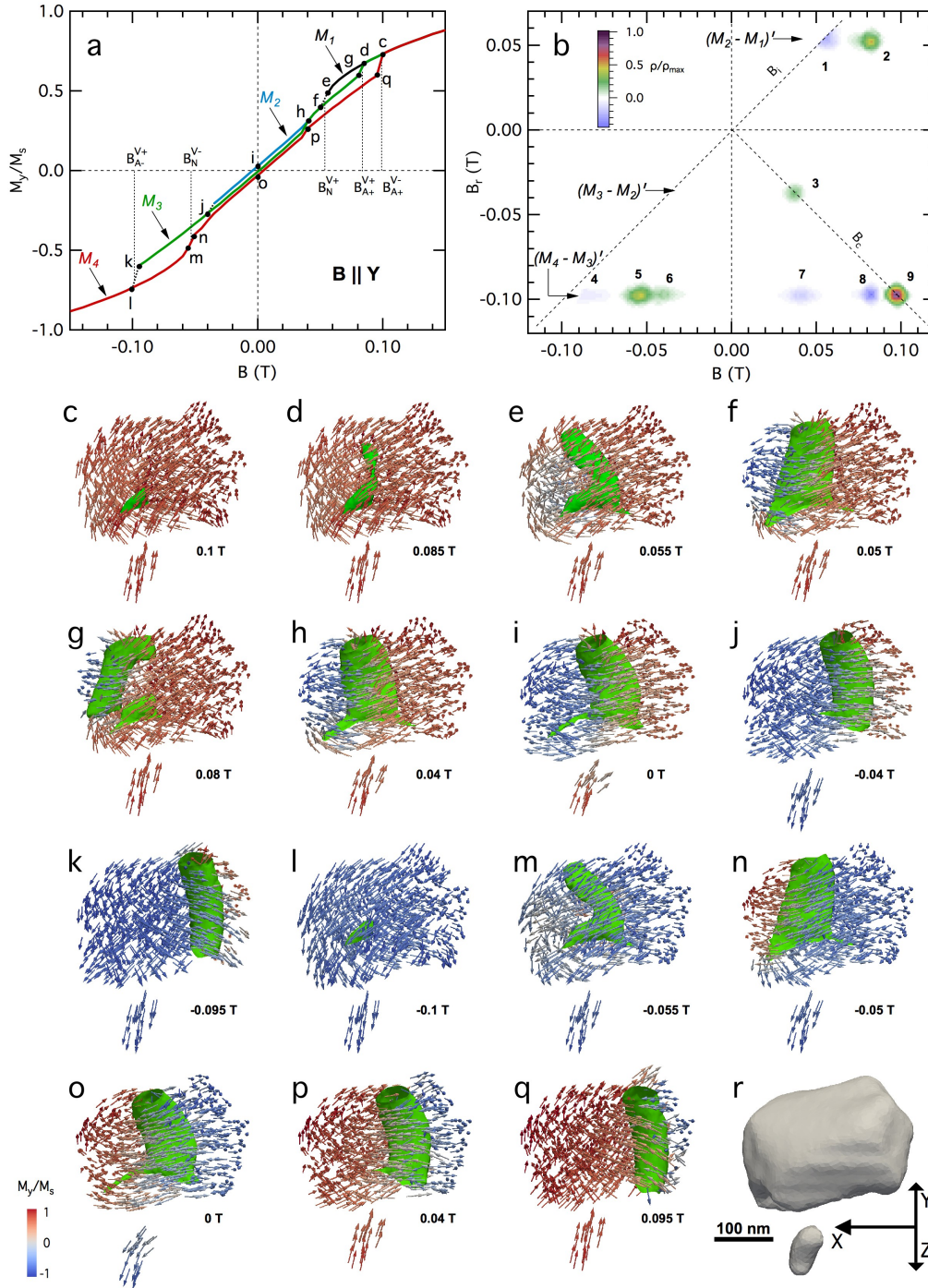


**Figure 1.** Magnetite layer in Glass Buttes obsidian. a) Examples of imagery acquired during the FIB slice and view protocol. b) Two views of the volume reconstructed via FIB-nanotomography. Particle sizes vary from  $\sim 100$  nm to  $>1$   $\mu\text{m}$ . The larger particles have formed through coalescence of smaller grains from neighboring nucleation sites during crystal growth.



949 **Figure 2.** a) FORC measurements of Glass Buttes obsidian sample. For clarity, only every 5th FORC is  
 950 plotted. b) FORC diagram resulting from processing the FORCs in (a) using the following smoothing parame-  
 951 ters:  $s_{c,0} = s_{b,0} = 9$ ,  $s_{c,1} = s_{b,1} = 9$ ,  $\lambda = 0.2$ . Contour interval is  $10^{-6} \text{ Am}^2/\text{T}^2$ . Dashed contour delineates  
 952 regions of the FORC distribution significant at the 0.05 level [Heslop and Roberts, 2012]. See text for de-  
 953 scription of the component features of the FORC fingerprint and the zones they occupy (labeled 1, 2, and 3).  
 954 The three zones are delimited by the diagonals of the FORC diagram, which represent the  $(B, B_r)$  coordinates.  
 955 c) Low temperature 2.5 T remanence measured on warming after two different pretreatments: cooling in field  
 956 (FC) and cooling in zero field (ZFC). d) Magnetic susceptibility as a function of temperature.



957 **Figure 3.** Micromagnetic FORC simulation of the gm1-gm2 ensemble with the field applied along Y. a)  
 958 Simulated FORCs: the 4 branches are labeled  $M_1$  to  $M_4$ . Letters indicate panels corresponding to micromag-  
 959 netic states at positions marked by black dots.  $B_N$  is the nucleation field, while  $B_{A+}$  and  $B_{A-}$  are annihilation  
 960 fields along ascending and descending branches, respectively. The  $V+$  and  $V-$  superscripts represent the  
 961 positive and negative saturation vortices. b) FORC diagram, processed using simple smoothing, with SF =  
 962 2.5. Positive and negative features (labeled 1-9, discussed in text) plot along three horizontal paths, labeled  
 963  $(M_2 - M_1)'$ ,  $(M_3 - M_2)'$ , and  $(M_4 - M_3)'$ , located at reversal fields ( $B_r$ ) where magnetization jumps have  
 964 occurred. The diagonals of the diagram are the  $B_c$  and  $B_i$  axes. c-q) Micromagnetic states corresponding to

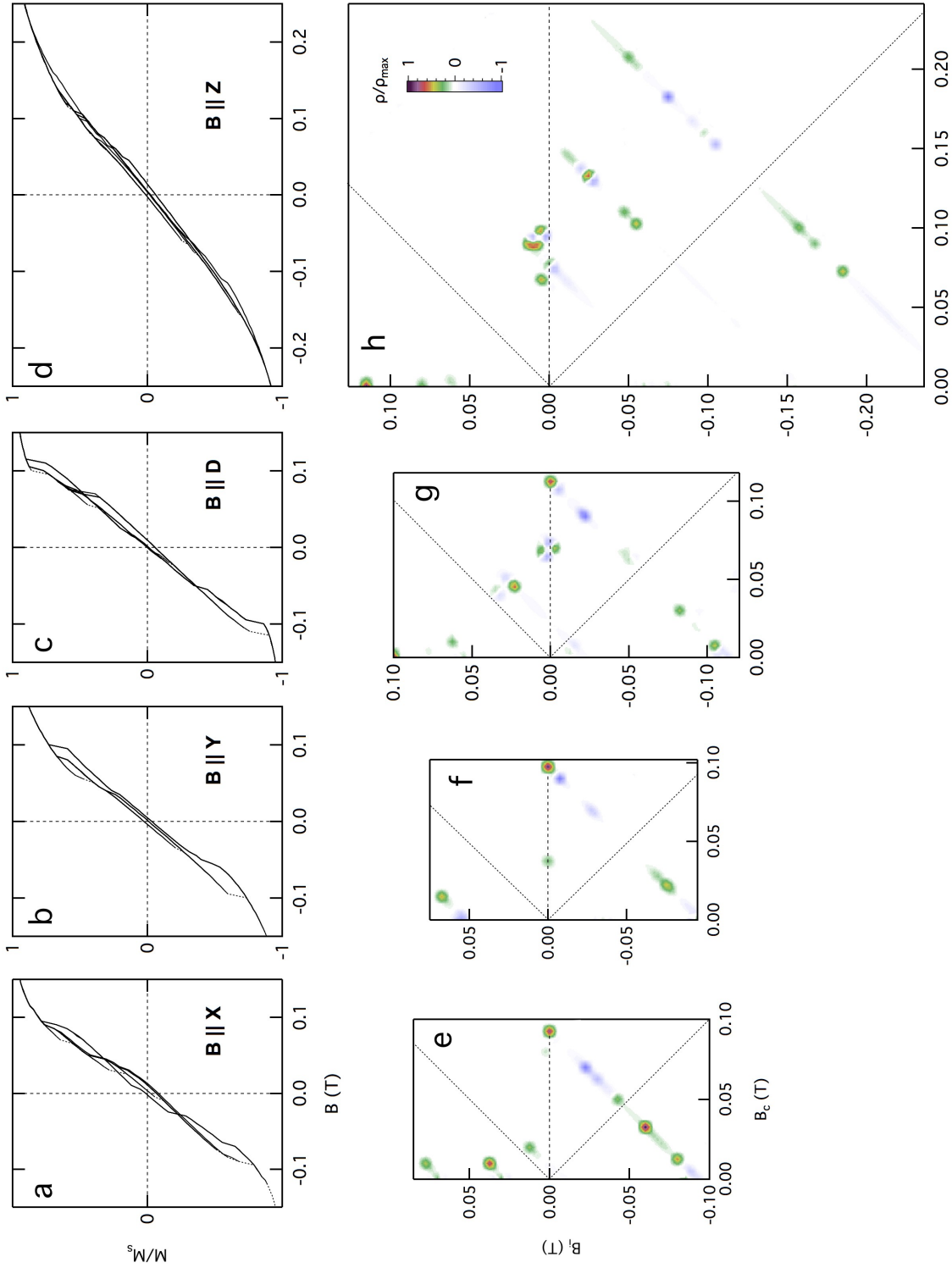
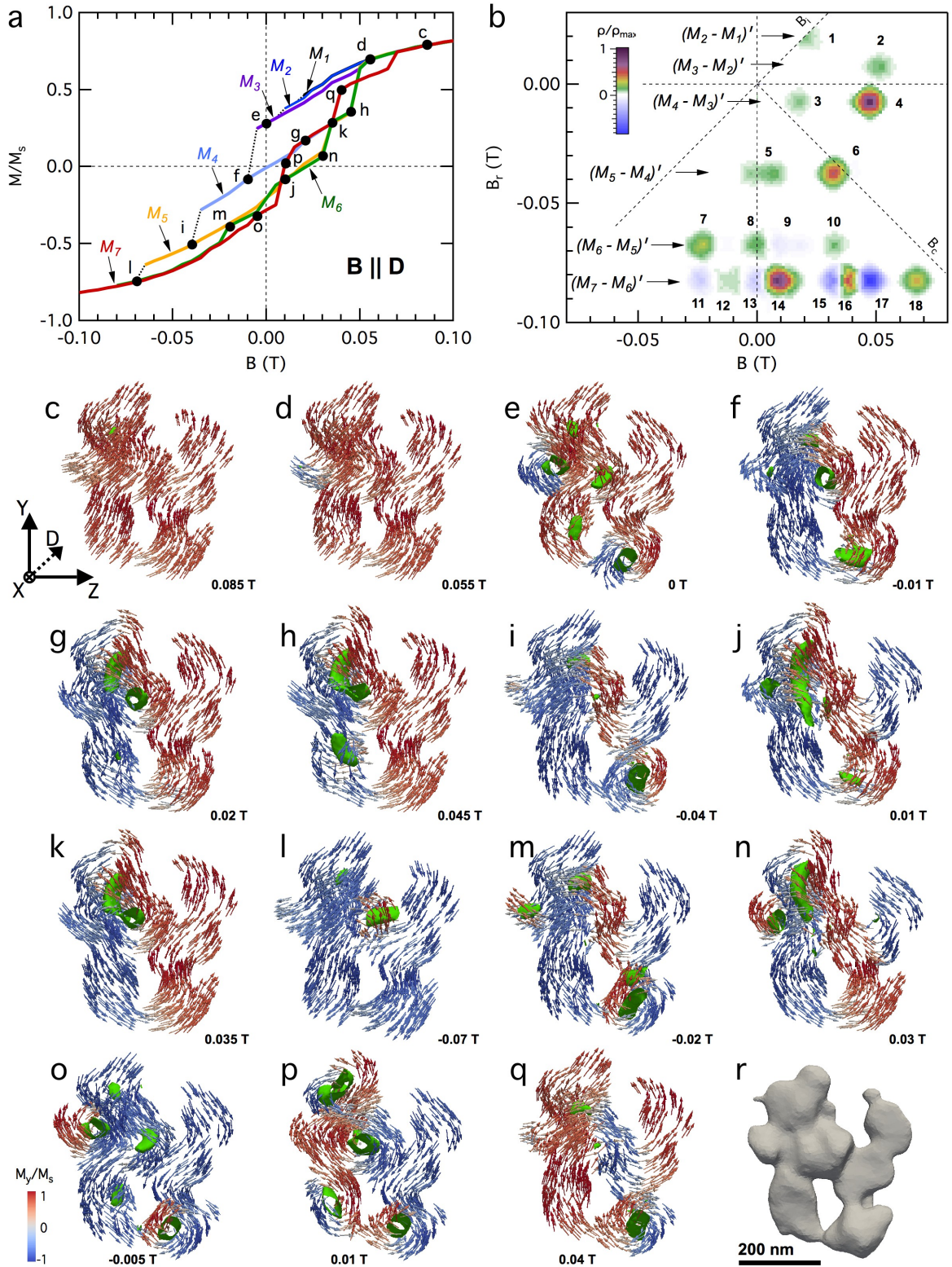
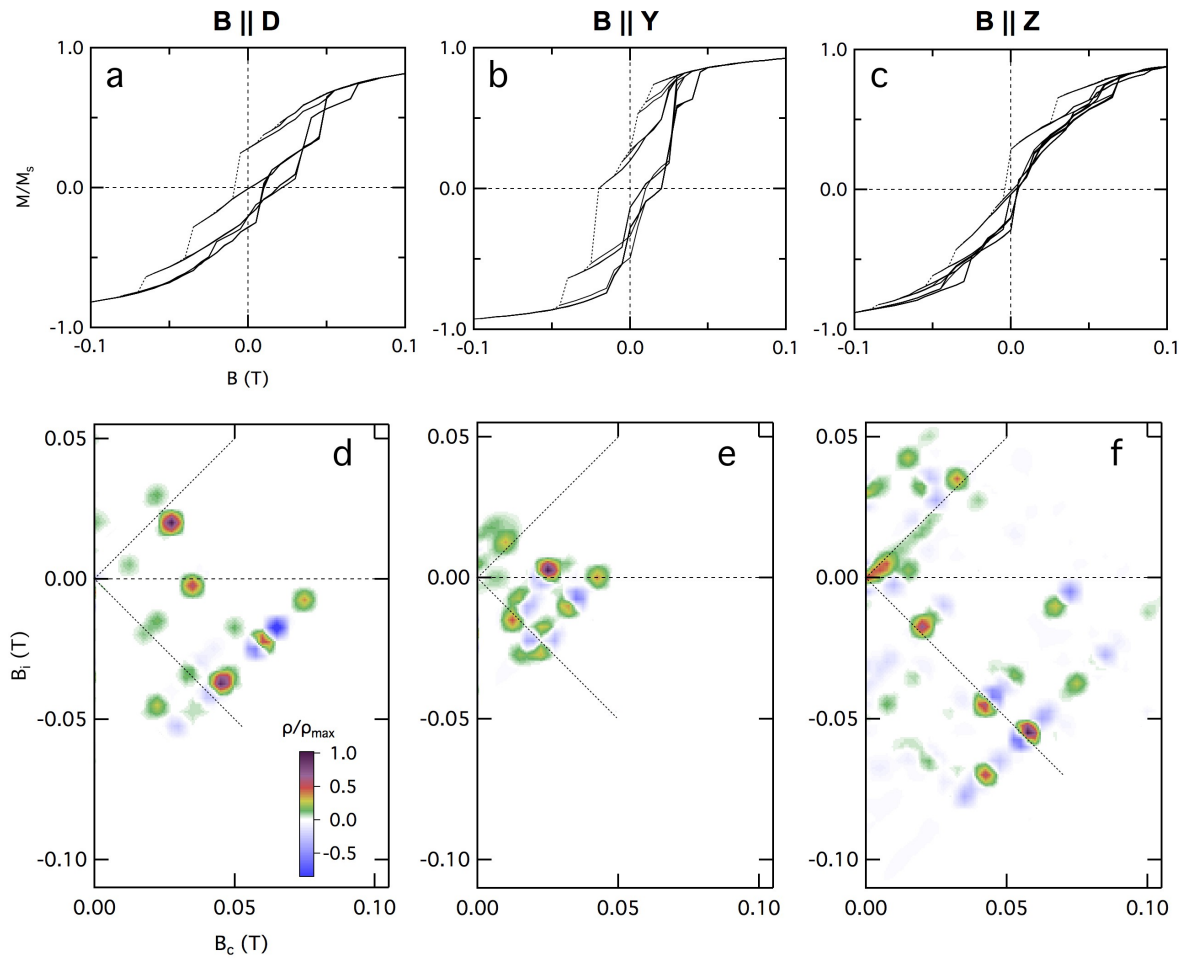


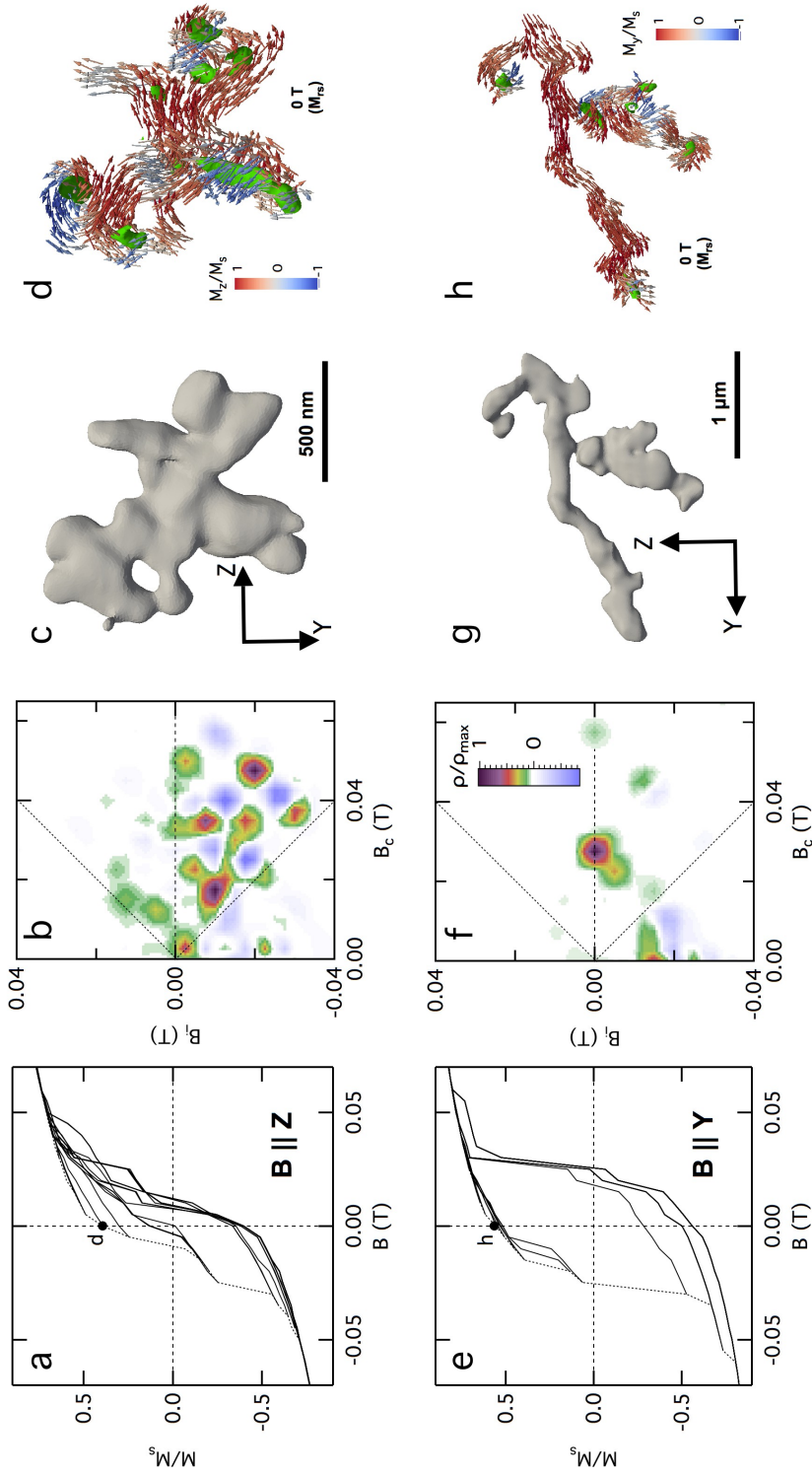
**Figure 4.** Simulated FORCs (a-d) and FORC diagrams (e-h) of the gm1-gm2 ensemble along four field directions: X (a, e), Y (b, f), Z (c, g), and D (d, h). Direction D is the diagonal of the coordinate system plotted in Fig. 3. SF = 2.5.



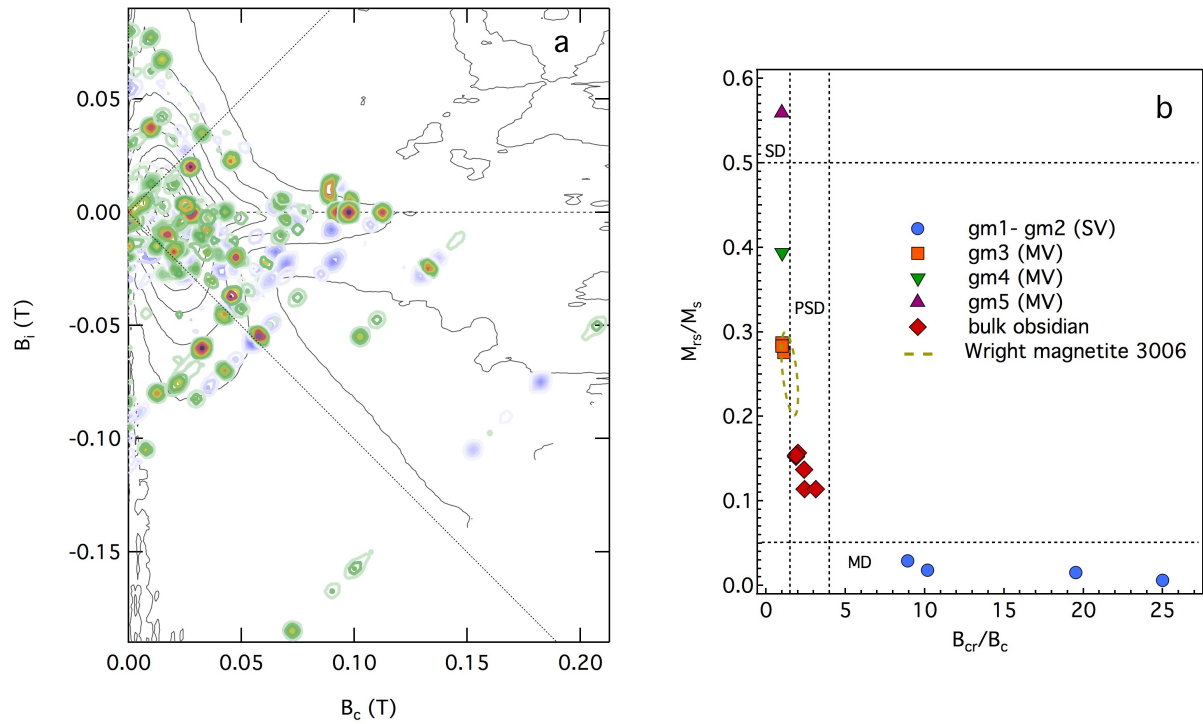
968 **Figure 5.** Micromagnetic FORC simulation of particle gm3 with the field applied along D. a) Simulated  
 969 FORCs: the 7 branches are labeled  $M_1$  to  $M_7$ . Letters indicate panels corresponding to micromagnetic states  
 970 at positions marked by black dots. b) FORC diagram, processed using simple smoothing, with SF = 2.5. Posi-  
 971 tive and negative features (labeled 1-18, discussed in text) plot along 6 horizontal paths (labeled  $(M_{j+1} - M_j)'$ ,  
 972  $1 \leq j \leq 6$ ) located at reversal fields ( $B_r$ ) where magnetization jumps have occurred. The diagonals of the dia-



976 **Figure 6.** Simulated FORCs (a-c) and FORC diagrams (d-f) of particle gm3 along three field directions: D  
 977 (a, d), Y (b, e), and Z (c, f). Direction D is the diagonal of the coordinate system, as seen in Fig. 5.  $SF = 2.5$



**Figure 7.** FORC simulations of particles gm4 (a-d, field applied along Z) and gm5 (e-h, field applied along Y): FORCs (a, e), FORC diagrams (b, f), particle meshes (c, g), and micromagnetic states at saturation remanent magnetization,  $M_{rs}$  (d, h). SF = 2.5



978 **Figure 8.** a) Positive and negative features from the all the FORC diagrams simulated in this study su-  
 979 perimposed onto the contours of the experimental FORC diagram shown in Fig. 2. b) Day diagram of the  
 980 nine simulations and six obsidian samples. Dashed ellipse indicates the range of values for Wright Co. mag-  
 981 netite 3006 (mean grain size  $1 \mu\text{m}$ ) hysteresis parameters [Yu, 2002; Carter-Stiglitz et al., 2001; Dunlop and  
 982 Carter-Stiglitz, 2006; Harrison et al., 2018].